

Matter Mixing in Core-collapse Supernova Ejecta: Large Density Perturbations in the Progenitor Star?

Jirong Mao^{1,2,5,6}, Masaomi Ono², Shigehiro Nagataki¹, Masa-aki Hashimoto², Hiroataka Ito¹, Jin Matsumoto¹, Maria G. Dainotti^{1,3}, Shiu-Hang Lee^{1,4}

jirong.mao@riken.jp

ABSTRACT

Matter mixing is one important topic in the study of core-collapse supernova (CCSN) explosions. In this paper, we perform two-dimensional hydrodynamic simulations to reproduce the high velocity ^{56}Ni clumps observed in SN 1987A. This is the first time that large density perturbation is proposed in the CCSN progenitor to generate Rayleigh-Taylor (RT) instability and make the effective matter mixing. In the case of a spherical explosion, RT instability is efficient at both C+O/He and He/H interfaces of the SN progenitor. Radial coherent structures shown in perturbation patterns are important for obtaining high velocity ^{56}Ni clumps. We can also obtain matter mixing features and high velocity ^{56}Ni clumps in some cases of aspherical explosion. We find that one of the most favorable models in our work has a combination of bipolar and equatorially asymmetric explosions in which at least 25% of density perturbation is introduced at different composition interfaces of the CCSN progenitor. These simulation results are comparable to the observational findings of SN 1987A.

Subject headings: Hydrodynamics — instabilities — nuclear reactions, nucleosynthesis, abundances — shock waves — supernovae: general

¹Astrophysical Big Bang Lab, RIKEN, Wako, Saitama 351-0198, Japan

²Department of Physics, Kyushu University, Fukuoka 812-8581, Japan

³Astronomical Observatory, Jagiellonian University, ul. Orla 171, Krakow 31-501, Poland

⁴Institute of Space and Astronautical Science (ISAS), Japan Aerospace Exploration Agency (JAXA), Kanagawa 252-5210, Japan

⁵Yunnan Observatory, Chinese Academy of Sciences, Kunming, Yunnan Province, 650011, China

⁶Key Laboratory for the Structure and Evolution of Celestial Objects, Chinese Academy of Sciences, Kunming, China

1. Introduction

Heavy elements in the universe can be released by core-collapse supernova (CCSN) explosions. It has been found in the observations of SN 1987A that some fast-moving ^{56}Ni clumps ejected outside have similar velocities of helium and hydrogen (e.g., Hanuschik et al. 1988). This phenomenon is called matter mixing in this paper. The radioactive decay of $^{56}\text{Ni} \rightarrow ^{56}\text{Co} \rightarrow ^{56}\text{Fe}$ (the half-lives of ^{56}Ni and ^{56}Co are 5.9 and 77.1 days, respectively) and the related energy heating of SN 1987A provide excellent opportunities to study matter mixing problems and explosion morphology. Early detections of hard X-ray emission (Dotani et al. 1987; Sunyaev et al. 1987) and gamma-ray lines from ^{56}Co (Matz et al. 1988; Leising & Share 1990) in SN 1987A indicate a high velocity component of radioactive ^{56}Ni from the CCSN explosive nucleosynthesis. The explosion energy of SN 1987A is given as $E/M_{\text{env}} = (1.1 - 1.5) \times 10^{50} \text{ erg } M_{\odot}^{-1}$ where M_{env} is the mass of the hydrogen-rich envelope in the supernova (SN) progenitor and the total mass of synthesized ^{56}Ni in SN 1987A is about $0.07 M_{\odot}$ (Shigeyama et al. 1988; Shigeyama & Nomoto 1990; see also Handy et al. 2014 for the summary of SN 1987A explosion energy). The mass of high velocity ^{56}Ni clumps was determined to be about a few times of $10^{-3} M_{\odot}$ (Utrobin et al. 1995) from the measurement of $\text{H}\alpha$ fine structure (Hanuschik et al. 1988). Haas et al. (1990) and Spyromilio et al. (1990) observed doppler-broadened line profiles of $[\text{Fe II}]$ in SN 1987A. Haas et al. (1990) found that the velocity can reach about $4,000 \text{ km s}^{-1}$, and 4 – 17% of the total ^{56}Ni has a high velocity larger than $3,000 \text{ km s}^{-1}$. Furthermore, the line profile is asymmetric, and its peak is located in the redshifted side of about $1,000 \text{ km s}^{-1}$ (Haas et al. 1990; Spyromilio et al. 1990). Another interesting radioactive element produced by the explosive nucleosynthesis is ^{44}Ti . Models of the spectrum and lightcurve of SN 1987A powered by ^{44}Ti have been presented (Fransson & Kozma 1993; Jerkstrand et al. 2011). Although the half-life of $^{44}\text{Ti} \rightarrow ^{44}\text{Sc} \rightarrow ^{44}\text{Ca}$ is about 59 years (the half-lives of ^{44}Ti and ^{44}Sc are 58.9 ± 0.3 years and 3.97 hr, respectively, see Ahmad et al. 2006), hard X-ray emission lines from the decay of ^{44}Ti in SN 1987A were also detected and the estimated mass of ^{44}Ti is $(3.1 \pm 0.8) \times 10^{-4} M_{\odot}$ (Grebenev et al. 2012). The inner ejecta of SN 1987A is heated by the radioactivity of ^{44}Ti (Kjær et al. 2010). Moreover, three-dimensional (3D) structures reconstructed by observations show that the inner ejecta of SN 1987A may lie in the plane of the equatorial inner ring (Kjær et al. 2010; Larsson et al. 2013; Sinnott et al. 2013). As the collision between this inner ejecta and the edge of inner ring may happen, this morphology can naturally explain the observed inner ejecta rebrightening (e.g., Gröningson et al. 2008, Dwek et al. 2010).

The physical mechanisms of CCSN explosions are under debate. In general, there are at least two interesting aspects of CCSN explosion mechanisms (e.g., Janka 2012; Kotake et al. 2012; Burrows 2013). In the framework of a neutrino heating mechanism, standing accretion shock instability (SASI, Blondin et al. 2003) and neutrino-driven convection (Herant et al.

1994; Burrows et al. 1995) were proposed to generate a globally anisotropic structure and enhance the effective heating. Many hydrodynamic simulations have been performed during recent years (e.g., Nordhaus et al. 2010; Suwa et al. 2011; Kuroda et al. 2012; Müller et al. 2012; Bruenn et al. 2013; Couch & Ott 2013; Hanke et al. 2013; Murphy et al. 2013; Ott et al. 2013, Wongwathanarat et al. 2013; Takiwaki et al. 2014). On the other hand, MHD effects can trigger a jet-like CCSN explosion, as shown in some numerical simulations (Kotake et al. 2004; Sawai et al. 2005, 2013; Burrows et al. 2007; Takiwaki et al. 2009).

So far, some tests to solve the matter mixing problems of CCSN explosions have been carried out under the hydrodynamic framework, and the explosive nucleosynthesis has been adopted in particular. Rayleigh-Taylor (RT) instability (or Richtmyer-Meshkov instability in the condition of entropy impulsive acceleration) can happen naturally in CCSN explosion models, and it plays a vital role on shock propagation and matter mixing. For example, it was found in early works that He/H and C+O/He layers in an SN progenitor can be unstable against strong RT instability (Ebisuzaki et al. 1989; Benz & Thielemann 1990). RT fingers first dominate at the H/He interface, and at late times are prominently shown at the He/C+O interface (Müller et al. 1991).

Perturbation in the progenitor star has been considered to be an origin of RT instability and this mechanism may be adopted to solve matter mixing problems. In principle, perturbations are related to the physics of convection and turbulence in the stellar interior. The integrated convection turnover time across the whole convective region is comparable to the nuclear timescale. This indicates that the composition in the CCSN progenitor is not homogeneous, thus the progenitor system has strong fluctuations (Bazan & Arnett 1998). Stellar convection is thought to make significant perturbations based on the dynamical simulations of progenitor stars (e.g., Bazan & Arnett 1994; Bazan & Arnett 1998; Meakin & Arnett 2007b; Arnett & Meakin 2011a). Bazan & Arnett (1994) suggested progenitor perturbations of density, temperature, pressure, and electron fraction in the order of 5%, 1%, 3%, and 0.08%, respectively. Arnett (1994) expected 2.5% of density perturbation and 0.8% of velocity perturbation in the oxygen shell of progenitor star. CCSN progenitor features were also explored by an extended work of density perturbation at the edges of metal convective zones (Bazan & Arnett 1998). Furthermore, some violent dynamic eruptions in the convective zones with simultaneous carbon and oxygen shell burning inside the progenitor star were found in 3D simulations, and about 10% of density perturbation was detected in those convective zones (Meakin & Arnett 2007b; Arnett & Meakin 2011a).

The position that RT instability occurs in the CCSN progenitor has also been discussed. Arnett et al. (1989) noticed the possibility that RT instability begins at the edge of the dense mass shell, where heavy elements mix with hydrogen through the He envelope. Müller et al.

(1991) mentioned that RT fingers form at both He/C+O and H/He interfaces. Nagataki et al. (1998) introduced velocity perturbation at the layer between He and H. Ellinger et al. (2012) found that this instability at He/H interface is caused by reverse shock. Hammer et al. (2010) and Kifonidis et al. (2003, 2006) found an instability at the Si/O interface, which was not shown in the results of Ellinger et al. (2012). Although all of instabilities at Si/O, He/C+O, and He/H interfaces were described by Kifonidis et al. (2003), the instability at the C+O/He boundary may be the most prominent one (Ellinger et al. 2012). This is consistent with the conclusion given by Kane et al. (2000).

It is expected that perturbations in the CCSN progenitor may generate or enhance the matter mixing. Simulations with introducing an initial density perturbation of 5% amplitude in the progenitor model failed to reproduce the high velocity ($> 3500 \text{ km s}^{-1}$) ^{56}Ni clumps (Herant & Benz 1991, 1992). On the other hand, the possibility of large perturbations in the CCSN progenitor has been investigated. The matter mixing can be reproduced by simulation models if 30% of the initial velocity perturbation and 30% of the initial energy perturbation are introduced in the CCSN progenitor (Yamada & Sato 1991). Nagataki et al. (1998) introduced 30% of velocity perturbation at the H/He boundary layer in the CCSN progenitor and obtained high velocity ($> 3000 \text{ km s}^{-1}$) ^{56}Ni clumps. However, the spacial resolution of these simulations is rather low. Three-dimensional simulations with different metallicities in the CCSN progenitor were also performed to develop RT instability (Joggerst et al. 2009, 2010a,b). It is interesting that large asymmetric structures during late times of a CCSN explosion may be originated by the significant perturbation that arises from an initial explosion itself, but not from merging RT structures.

The asymmetric effect of a CCSN explosion is also involved as an important point for the matter mixing. Nagataki et al. (1998) and Nagataki (2000) found that asymmetric or jet-like explosions can effectively change the velocity distribution of ^{56}Ni . Hungerford et al. (2003, 2005) performed 3D smoothed particle hydrodynamics (SPH) simulations and compared the difference between symmetric and asymmetric CCSN explosions. They confirmed that an asymmetric explosion makes the matter mixing in supernova ejecta, although high velocity ^{56}Ni clumps could not be reproduced. Kifonidis et al. (2003) comprehensively discussed RT instability and explosion evolution in one-dimensional (1D) and two-dimensional (2D) cases. Introducing low-mode perturbation in a CCSN explosion progenitor may reproduce high velocity ($> 3300 \text{ km s}^{-1}$) ^{56}Ni clumps (Kifonidis et al. 2006), although robust conclusions of 2D simulations were further discussed by Gawryszczak et al. (2010). Three-dimensional simulations of CCSN explosions were also performed by Hammer et al. (2010), and high velocity ^{56}Ni could be reproduced. However, their models neglected the effect of matter fallback into the compact remnant. As recently suggested by Ono et al. (2013), not only perturbations in the SN progenitor but also asymmetric explosions (clumpy morphologies

in explosions) may be necessary to reproduce the observed high velocity ^{56}Ni clumps of SN 1987A.

In this paper we focus on RT instability as one possible solution of matter mixing problems in SN 1987A. We have already performed 2D hydrodynamic simulations to examine the matter mixing of CCSN (see Paper I). If a large radial velocity perturbation of 30% amplitude is introduced just before the shock wave reaches the hydrogen envelope of the progenitor star, high velocity ^{56}Ni clumps of $3,000 \text{ km s}^{-1}$ may be reproduced, in the case of bipolar explosion. This indicates that RT instability originating from large perturbations in the progenitor may be one reason for the matter mixing in a CCSN explosion. Here, we further extend the work in Paper I. In particular, this is the first time that large density perturbation is systematically considered in a CCSN progenitor to make strong RT instability, and consequently dig out a part of inner heavy elements to outer layers during CCSN explosion. Here, we mention some possible motivations of the large density perturbations introduced in our CCSN progenitor. The global turbulent feature of the CCSN progenitor interior was explored (Meakin & Arnett 2007a; Arnett et al. 2009; Arnett & Meakin 2011a,b; Viallet et al. 2013), and it was realized that a realistic progenitor model is crucial for CCSN explosion (Smith & Arnett 2014). In this paper, we adopt the CCSN progenitor that has been successfully used to produce the lightcurve, ^{56}Ni mass, and explosion energy of SN 1987A (Shigeyama et al. 1987, 1988; Hashimoto et al. 1989; Shigeyama & Nomoto 1990). Then, we introduce large density perturbations to this progenitor. We suggest that this progenitor with a large density perturbation may be physically equivalent/corresponding to a realistic model with a global turbulent feature and strong dynamic instabilities. Furthermore, Figure 2 shows that the radial coherent features at large scales exist in some of our perturbation patterns. These radial coherent features are important for reproducing the matter mixing of SN 1987A. The coherent features shown in our perturbation patterns may capture the similar behavior driven by the turbulent convection in the stellar interior (Meakin & Arnett 2007a; Arnett et al. 2009; Arnett & Meakin 2011a,b; Viallet et al. 2013). Moreover, Smith & Arnett (2014) argued two important effects of the hydrodynamic instability and turbulence in the progenitor model: (1) finite amplitude fluctuations in velocity and temperature, and (2) nonlinear interaction with nuclear burning during the latest stages of the stellar evolution. These effects are not included in current stellar evolution models. Smith (2007) claimed that SN 1987A is related to the luminous blue variable (LBV), which shows violent dynamical eruption or enhanced mass loss prior to the core-collapse. This invokes large density perturbation in the hydrogen envelope of the CCSN progenitor. We also propose Betelgeuse as an observational example: The clumpy structure in the inner envelope may be related to the giant convection cells of the outer atmosphere (Decin et al. 2012). The convection pattern can be also unveiled (Montarges et al. 2014). These observational evidences also suggest

large density perturbation in the hydrogen envelope of the CCSN progenitor.

We suggest some physical factors—such as C+O layer convection, non-radial pulsations in LBV stars, cool hydrogen envelopes, and convection-driven asymmetries in the deep interior— are affecting the development of RT instability and the matter mixing of SN 1987A. Although we introduce large density perturbations in the progenitor model as a major cause to develop RT instability and produce the matter mixing in this paper, there are many pathways to the final asymmetries after the shock breakout. We focus on perturbations in the progenitor star, and its growth due to RT instability during the shock wave propagation. As mentioned, perturbations could be introduced by combinations of different sources, such as convection in very deep, cool hydrogen envelopes; convective shell burnings in the deep interior; and nonlinear, non-radial pulsations in an LBV star. Aside from the origins of the perturbations, the growth of RT instability is affected by the progenitor structure. For giant RT fingers, a large hydrogen envelope, as in normal red supergiant (RSG) stars, is required (e.g., Wongwathanarat et al. 2015). On the other hand, RT instabilities in Wolf-Rayet progenitors may be significantly reduced by the lack of an H/He boundary with a strong density gradient. However, deeper asymmetries stemming from the RT instabilities at inner composition boundaries and/or an aspherical explosion could still produce structure. Because the progenitor of SN 1987A is known to be a blue supergiant (BSG), which had a compact hydrogen envelope, it is difficult to produce prominent RT fingers compared to those of RSG stars. In addition, to dig out the innermost ejecta to outer layers, other factors—such as the compactness of the C+O shell, the density structure of He shell, and the density gradient at He/H boundary—may also be important (Wongwathanarat et al. 2015).

We propose a large density perturbation in the progenitor model as follows: We test three cases of perturbations for spherical explosion. For all cases, the amplitude of perturbations are randomly assigned, but the length scale of the perturbations are different. First, perturbations are introduced at the interfaces of different composition layers, with an exponential decay of its amplitude in the radial direction. At each boundary layer, the length scale of the perturbation in the angular direction is controlled by a fixed wave number. In this case, perturbations have the radial coherent structure. Second, the perturbation length scale in the radial direction is proportional to the density scale height determined by the progenitor model. The perturbation length scale in angular direction is controlled by a fixed wave number. Third, we constrain the perturbation length scale in both radial direction and angular direction, as it is proportional to the density scale height. All of these perturbation modes are comprehensively described in Section 2.3 and illustrated in Figures 1 and 2. We also test three cases for aspherical explosion under the condition that perturbations are introduced at interfaces of different composition layers. First, we take the case that explosion along the polar direction is stronger than that along the equatorial direction. This

corresponds to a bipolar or jet-like SN explosion. Second, we propose the case of an SN explosion that is asymmetric to the equatorial plane. Third, we combine the two cases to take into account both bipolar and equatorially asymmetric effects of the CCSN explosion. The observed [Fe II] line in SN 1987A shows an asymmetric feature in the velocity profile (Haas et al. 1990; Spyromilio et al. 1990). The observation of SN 1987A in 3D structure presents an elongated morphology (Kjær et al. 2010). These observational evidences invoke us to make a combination of mildly bipolar and equatorially asymmetric explosions. In our work, we concern the radial velocity profile and line of sight velocity profile of ^{56}Ni , the total ejected mass of ^{56}Ni , and the mass of high velocity ($> 3000 \text{ km s}^{-1}$) ^{56}Ni . We also discuss the total ejected mass of ^{44}Ti and the related explosion energy. In Section 2, we review the procedures of the numerical simulation presented in Paper I. Numerical simulation methods and the progenitor star are briefly described and many density perturbation modes are given in detail. In Section 3, we comprehensively show the matter mixing results of ^{56}Ni in our simulations. Some important issues associated with our results are discussed in Section 4. Finally, we summarize our achievements in Section 5.

2. Numerical Simulations

We now briefly describe numerical methods, initial conditions, and progenitor model, which are presented in Paper I. We list several key points for our simulation models in Section 2.1 and 2.2. We extend the work of Paper I to explore the possibility of reproducing high velocity ^{56}Ni clumps by using the progenitor with large density perturbation, and comprehensive perturbation modes are presented in Section 2.3.

2.1. Numerical Arrangements and Initial Conditions

We perform an adaptive mesh refinement (AMR) hydrodynamic code, FLASH (Fryxell et al. 2000), and a 2D spherical coordinate (r, θ) is adopted. The initial computation domain covers the region with a radius of $1.4 \times 10^8 \text{ cm} < r < 3.0 \times 10^9 \text{ cm}$ and an angle of $0 < \theta < \pi$. The outer boundary of the progenitor model is limited at $r = 3.4 \times 10^{12} \text{ cm}$, which corresponds to the surface of the hydrogen-rich envelope. A wind component is added beyond this radius. The base-level grid points are $48(r) \times 12(\theta)$ and the maximum refinement level is set to be 7. Thus, the effective maximum numbers of grid points are $3072(r) \times 768(\theta)$. The minimum effective cell sizes are about 10 km and 0.23 deg in radial direction and angular direction, respectively. As the SN shock propagates and reaches close to the radial outer boundary, the computation domain is extended via remappings. When the physical values of the extended

regions are set to the values of the progenitor model, 44 remappings are required. We use the monotonic cubic interpolation scheme to interpolate physical values (Steffen 1990). The computational cost is about 20 thousand CPU hr for each simulation model.

The remapping and boundary conditions applied in this work were presented in Paper I. If the forward shock and/or RT fingers reach close to the radial outer boundary (approximately 20% of the radial computational domain from the radial outer boundary), the radial size of the computational region is extended by a factor of 1.2. At the radial inner boundary, a “reflection” boundary condition is employed at the start of simulation. After the forward shock has reached the composition interface of C+O/He (corresponding to the radius of 6×10^9 cm), it is switched to a “diode” boundary condition that allows matter to flow out of the computational domain, but inhibits it from entering the computational domain through the inner boundary in order to include the effect of matter fallback. Although changing the switch timing can somewhat affect the degree of the innermost matter fallback, we fix the switch timing to make sure that the mass of ^{56}Ni that remains in the computational domain does not become too small compared with that for SN 1987A. At the radial outer boundary, we adopt the “diode” boundary condition over the simulation. In the angular direction, we take the “reflection” boundary condition. Meanwhile, the mass inside the inner computation domain is regarded as a point source, and both the point source gravity and spherically averaged self-gravity are considered. The Helmholtz equation of state (EOS) is adopted for our simulations, whereas a modified ideal gas and radiation EOS is used for a very low density region, and we blend the two kinds of EOS at the transition density region (see Paper I for the details).

Explosive nucleosynthesis is applied and we obtain the following elements from FLASH code: n, p, ^1H , ^3He , ^4He , ^{12}C , ^{14}N , ^{16}O , ^{20}Ne , ^{24}Mg , ^{28}Si , ^{32}S , ^{36}Ar , ^{40}Ca , ^{44}Ti , ^{48}Cr , ^{52}Fe , ^{54}Fe , and ^{56}Ni . Advection equations are solved to trace the distribution of these elements. Energy depositions due to the radioactive decay of ^{56}Ni to ^{56}Fe are included, as described in Paper I. However, some isotopes of iron group elements (e.g., ^{57}Ni and ^{58}Ni) are not included in the original FLASH code. Therefore, the masses of ^{56}Ni and ^{44}Ti obtained by FLASH code may be overestimated. In order to clarify the effect of this limited nuclear reaction network on the mass of heavy elements, an explosive nucleosynthesis calculation with a large nuclear network is performed as a post-process. We stress this issue in Section 4. The process is presented in the Appendix.

2.2. Progenitor Model

The progenitor model of CCSN explosion adopted in this paper is a $16.3 M_{\odot}$ BSG star with $6 M_{\odot}$ helium core and $10.3 M_{\odot}$ hydrogen envelope. This progenitor model has a radius set as 3.4×10^{12} cm, and has been successfully adopted for reproducing the lightcurve, explosion energy, and total ^{56}Ni mass ($0.07 M_{\odot}$) of SN 1987A (Shigeyama et al. 1987, 1988; Nomoto & Hashimoto 1988; Shigeyama & Nomoto 1990). A wind component with the density profile of $\rho \propto r^{-2}$ is added and the uniform temperature of $T = 10^4$ K is adopted. The inner density of the wind component is 3.0×10^{-10} g cm $^{-3}$. The wind component is extended to the radius of 4.5×10^{12} cm and simulations are carried out until just before the shock waves reach the radius. The density of the wind component is smoothly connected to that of the stellar surface. If we assume that the wind velocity is 15 km s $^{-1}$, the mass loss rate is $1.8 \times 10^{-3} M_{\odot}$ yr $^{-1}$; this value is larger than $1.0 \times 10^{-5} M_{\odot}$ yr $^{-1}$ used in Gawryszczak et al. (2010). We restrict our simulation to just after the shock breakout, and the selected wind profile does not affect the matter mixing.

We set the total input energy to be 2.5×10^{51} erg in most simulation models and divide this input energy into two equal parts: kinetic energy and thermal energy. The final explosion energy is related to the input energy. Modification of total input energy value is also attempted in the two simulation models.

Si, C+O, He, and H layers are settled as an onion-like structure in this progenitor. The outer boundary of the Si-rich layer is at the radius of 3×10^8 cm, the interface between C+O and He core is at 6×10^9 cm, and the hydrogen envelope begins at 5×10^{10} cm. It is also noted that oxygen shell burning is limited at 3×10^9 cm (Arnett 1994; Bazan & Arnett 1998). Therefore, we propose that these numbers are four critical radii in the progenitor star.

2.3. Explosion and Density Perturbation Modes

2.3.1. Spherical Explosion of SC1, SC2, and SC3

In this subsection, we introduce three density perturbation modes that affect matter mixing in a spherical CCSN explosion. From the dynamical simulations of oxygen shell burning (Bazan & Arnett 1998; Meakin & Arnett 2007b), density perturbations of $\delta\rho/\rho \sim 10\%$ could be introduced at the boundaries of the convective shell burning. We assume that density perturbations are prominently introduced at the boundaries of shell burnings, and further assume perturbations with large amplitude (up to 50%) to obtain successful matter mixing. Then, we consider density perturbations at four critical radii (3×10^8 cm

at Si/C+O interface, 3×10^9 cm at oxygen shell burning position, 6×10^9 cm at C+O/He interface, and 5×10^{10} cm at He/H interface), which roughly correspond to the boundaries of shell burnings in the progenitor. Density perturbation at each critical radius with the shape of $1 + \epsilon[2 \text{rand}(m\theta/\pi) - 1]$ in the angular direction is given, where rand is the random number within the range between 0 and 1, and is a function of θ . We take $m + 1$ random numbers at sample points, $\theta = 0, \pi/m, 2\pi/m, \dots, (m-1)\pi/m, \pi$. The random number for an arbitrary θ is obtained by an interpolation with the values of adjacent sample points, and ϵ is the amplitude of the perturbation. The amplitude has an exponential decay in the radial direction and can be presented as $\epsilon = \epsilon_0 \exp(-|r - r_0|/r_0)$, where ϵ_0 is the amplitude at each boundary layer and r_0 is the radius of the certain boundary. We call this case SC1. Thus, two parameters, ϵ_0 and m , are involved in SC1. In order to understand the perturbation effect at each boundary on the matter mixing, we perform four more one-by-one boundary perturbation models, in which perturbations at the Si/C+O interface, the C+O/He interface, the He/H interface, and both C+O/He and He/H interfaces are considered, respectively. The RT instabilities at the H/He and He/C+O boundaries can be generated by the passage of the shock and/or reverse shock, and the condition of RT instability ($\nabla\rho \cdot \nabla p < 0$) was given by Chevalier (1976). The growth rate of RT instabilities at H/He and He/C+O interfaces has been investigated (e.g., Ebisuzaki et al. 1989; Paper I) and such interfaces are unstable against RT instabilities after the passage of the shock waves. The four one-by-one boundary perturbation models are used to see which boundaries are critical for the matter mixing. In particular, we see the radial coherent structure in the perturbation pattern (Figure 2) that was obtained from large density perturbations imposed on those interfaces of the progenitor, which is important to the matter mixing of SN 1987A.

Besides the possibility of large density perturbations at interfaces of different composition layers, we propose that perturbations may also be introduced at any position in the progenitor. Although this global perturbation is not motivated by a known physical process, if the progenitor of SN 1987A was an LBV, such a perturbation might have existed. We propose the cases of SC2 and SC3, which are two different perturbation modes, to search the parameter space and explore the potential impacts. In the case of SC2, the density perturbation may be related to the density distribution of the progenitor star. We derive the density scale height $H(r)$, which can be presented as $H(r) = |dr/d \ln\rho|$. We assume that the radial length scale of the density perturbation $l_r(r)$ is proportional to the density scale height $H(r)$. For simplicity, we introduce a scaling factor f of $l_r(r) = fH(r)$. If we adopt $f = 5$ in a simulation model, we can obtain the radial coherent structure shown in Figure 2. A simulation model of $f = 1$ is also applied to compare with the corresponding model of $f = 5$. For a given radius, the angular length scale of the density perturbation is $l_\theta(r) = r\pi/m$, and we fix the number of m . We take random numbers at 2D sample points at intervals

of $l_r(r)$ and $l_\theta(r)$. The perturbation at arbitrary (r, θ) is given by $1 + \epsilon_0[2 \text{ rand}(r, \theta) - 1]$, where the random number is obtained by an interpolation with the values of neighboring sample points. In the case of SC2, the perturbations are modulated not only in the angular direction but also in the radial direction. Thus, three parameters, ϵ_0 , m and f , are involved in the case of SC2.

Third, we assume that the length scales of the perturbation in both the radial and angular direction, $l_r(r)$ and $l_\theta(r)$, respectively, are proportional to the density scale height $H(r)$. In other words, we assume $l_r(r) = fH(r)$ and $l_\theta(r) = fH(r)$. We take random numbers at 2D sample points at intervals of $l_r(r)$ and $l_\theta(r)$. The perturbation at arbitrary (r, θ) is given by $1 + \epsilon_0[2 \text{ rand}(r, \theta) - 1]$, where the random number is obtained by an interpolation with the values of the neighboring sample points. We call this case SC3. For SC3, two parameters, ϵ_0 , and f , are involved¹.

The density scale height, $H(r)$, of the progenitor and the ratio between r and $H(r)$ as a function of radius is illustrated in the upper panel of Figure 1. We can see that $H(r)$ is roughly proportional to r and the ratio $r/H(r)$ ranges between 2 and 8. The exception is the case for the regions around the stellar surface. In addition, $H(r)$ tends to be small around the composition interfaces of C+O/He and He/H. Moreover, we show the radial perturbations involved with the cases of SC2 and SC3 in the lower panel of Figure 1. We take the perturbation mode of SC3 ($\epsilon_0 = 50\%$ and $f = 1$) as an example, and see that the amplitude of the density perturbation in the radial direction is randomly distributed. Distributions of the 2D density perturbation clumps with amplitude $\epsilon_0 = 50\%$ for SC1, SC2, and SC3 are shown in Figure 2. For the case of SC1, perturbations are introduced around the critical radii, and angular perturbation is adjusted by the number of m . Perturbations extend from the chosen radii in both upward and downward directions. For SC2, perturbations are adjusted in angular direction and radial direction by m and f , respectively. For SC3, perturbations in both angular direction and radial direction are adjusted by the same number of f . Thus, from these perturbation patterns, we see that the coherent structure in the radial direction shown in some panels of Figure 2 plays a key role to reproduce high velocity ^{56}Ni clumps. In particular, we notice that the density perturbations

¹Before we perform simulations of SC1, SC2, and SC3, one simple case, “Basicmodel”, is considered. In this case, we introduce density perturbations at the four critical radii in the progenitor star as mentioned in SC1. However, we set the amplitude of the density perturbation at each critical radius by the way of $\epsilon = \epsilon_0 \exp(-|r - r_0|/h)$, where $\epsilon_0 = 0.5$, and h corresponds to the density scale height at each critical radius. From the function $H(r)$, we have $h_1 = 2.2 \times 10^8$ cm, $h_2 = 1.2 \times 10^9$ cm, $h_3 = 2.0 \times 10^9$ cm, and $h_4 = 2.0 \times 10^{10}$ cm at each critical radius, respectively. Density perturbation at each critical radius in angular direction is as same as that given in SC1. In this simple case, we cannot reproduce high velocity ^{56}Ni clumps. Then, we turn to complicated cases of SC1, SC2, and SC3 in the spherical explosion to reproduce the matter mixing.

driven by the turbulent convection in stellar interiors show the coherent feature on large scales, and wave numbers have an order of the circumference at the outer boundary divided by the depth of the convection zone (Meakin & Arnett 2007a; Arnett et al. 2009; Arnett & Meakin 2011a,b; Viallet et al. 2013). The coherence shown in our perturbation patterns with $m = 8$ can capture a similar feature.

2.3.2. *Aspherical Explosion*

The density perturbation modes mentioned in Section 2.3.1 are under the condition of spherical explosion. Because the observations of SN 1987A indicate an aspherical explosion, we can mimic some aspherical explosion cases that were adopted in Paper I. All of the following aspherical explosion models are under the case of SC1 density perturbation mode.

We take the initial radial velocity $v_r \propto r[1 + \alpha \cos(2\theta)]/(1 + \alpha)$ that was written as Equation (7) of Paper I. Through this function form, we can consider a bipolar explosion. In order to represent the bipolar explosion proposed by Nagataki et al. (1997, 1998), Nagataki (2000), and Paper I, we obtain the ratio of the radial velocity along the polar direction to that along the equatorial plane as $v_{\text{pol}}/v_{\text{eq}} = (1 + \alpha)/(1 - \alpha)$, where α is the parameter to determine the degree of asymmetry ($\alpha = 0$ corresponds to a spherical explosion). In this paper, α is set to be $3/5$, i.e. $v_{\text{pol}}/v_{\text{eq}} = 4$.

We also propose the asymmetric feature of the CCSN explosion to the equatorial plane as mentioned in Paper I (e.g., due to neutrino-driven explosion aided by SASI; Suwa et al. 2010). An equatorially asymmetric explosion is mimicked by changing the normalization of the radial velocity across $\theta = \pi/2$. We define the initial radial velocity at $\theta = 0$ and that at $\theta = \pi$ as v_{up} and v_{down} , respectively. We adjust the normalization so that $v_{\text{up}}/v_{\text{down}} = 1.8$. If we take $v_{\text{up}}/v_{\text{down}} = 2$, as given by Paper I, the estimated neutron star kick velocity becomes larger than that typical of young pulsars. Therefore, we adopt a smaller value for $v_{\text{up}}/v_{\text{down}}$ in this paper.

We can further combine the cases of bipolar explosion and equatorially asymmetric explosion together as a case of global asymmetric explosion. The combined global asymmetric explosion model may be used to examine SN 1987A explosion, as indicated by the asymmetric feature of [Fe II] line (Haas et al. 1990; Spyromilio et al. 1990) and the elongated morphology (Kjær et al. 2010) in SN 1987A.

3. Results

Our 2D hydrodynamic simulation results on the matter mixing of CCSN explosions are presented in this section. We list those parameters adopted in our simulation models in Table 1. Some major simulation results are listed in Table 2.

3.1. Spherical Explosion

We first present our simulation results for SC1. The results of the case with the perturbation amplitude $\epsilon_0 = 50\%$ and $m = 8$ are shown in Figure 3, whereas the results of the case with the perturbation amplitude $\epsilon_0 = 50\%$ and $m = 20$ are shown in Figure 5. We show density distribution, distribution of the ^{56}Ni mass fraction, radial velocity of several elements, and line of sight velocity profiles of ^{56}Ni , respectively². We clearly see that prominent RT fingers are formed and distributions of ^{56}Ni have anisotropic structures. Although most ^{56}Ni is within the inner part of the contour, we see that the RT fingers of ^{56}Ni are beyond the radial velocity of $3,000 \text{ km s}^{-1}$. The matter mixing happens, as we can see in radial velocity profiles. The line of sight velocity of ^{56}Ni is extended beyond $3,000 \text{ km s}^{-1}$, and high velocity ^{56}Ni clumps are reproduced. The perturbation modes of SC1 show a prominent coherent structure in radial direction (Figure 2), which we believe is important to reproduce high velocity ^{56}Ni clumps. A different set of random numbers may induce different results. To test this, we use the model of SC1p50m8 with a different set of random numbers and run the simulation again. We obtain the following results: total ^{56}Ni mass is $0.15 M_\odot$; high velocity ($> 3000 \text{ km s}^{-1}$) ^{56}Ni is 21.7% ; total ^{44}Ti mass is $2.1 \times 10^{-4} M_\odot$. Thus, our simulation results using this different set of random numbers are consistent with those of the original one. We plot the final density distribution, final distribution of ^{56}Ni mass fraction, radial velocity profile, and line of sight velocity profile of ^{56}Ni with different observational view angles in Figure 4.

The perturbation mode in the angular direction is dominated by the parameter m . Figures 3 and 5 show that different values of parameter m provide different RT fingers: More RT fingers in the angular direction are developed if we take a larger value of m . However, as high velocity ^{56}Ni clumps are mainly determined by the strong coherent structure in the radial direction, a larger percentage number of high velocity ^{56}Ni can be obtained by the simulation models with a smaller number of m .

²In this paper, for simplicity, the mass distributions of elements as a function of radial velocity at the ends of simulation time are called radial velocity profiles, and mass distributions of elements as a function of line of sight velocity at the ends of simulation time are called as line of sight velocity profiles.

In order to investigate the effect of the perturbation amplitude on the matter mixing of SN 1987A, simulations with 10% of density perturbation are also performed in the case of SC1. We show the results using parameter $m = 20$ as an example in Figure 6. Density distribution, distribution of ^{56}Ni mass fraction, radial velocity profiles of several elements, and line of sight velocity profiles of ^{56}Ni are given, respectively. Although RT instability is developed at the last stage, ^{56}Ni has roughly spherical distribution. We see that line of sight velocity of ^{56}Ni is limited within $2,000 \text{ km s}^{-1}$, and the mixing of the innermost elements (e.g., ^{56}Ni and ^{44}Ti) into high velocity ($> 3,000 \text{ km s}^{-1}$) regions has failed. We conclude that a density perturbation as small as 10% cannot reproduce the high velocity ^{56}Ni clumps of SN 1987A.

It is interesting to examine which boundary layer where density perturbation occurs is important for the matter mixing. We perform three simulation models in which perturbations are introduced at a single composition (Si/C+O, C+O/He, He/H) interface. One simulation model with perturbations at both C+O/He and He/H interfaces is also performed. The parameters of $m = 20$ and $\epsilon_0 = 50\%$ are set for each simulation model. We do not obtain high velocity ^{56}Ni when the density perturbation is introduced at the boundary layer between silicon and oxygen. If density perturbation is introduced at the C+O/He interface or He/H interface, high velocity ^{56}Ni clumps appear. However, the mass of high velocity ^{56}Ni is only about 0.7% of the total ^{56}Ni produced by the CCSN explosion, which is less than the observational value ($> 4\%$, Haas et al. 1990). If we take perturbations at both C+O/He and He/H interfaces, high velocity clumps of ^{56}Ni are successfully obtained. These results indicate that most effective density perturbations for the matter mixing occur at both C+O/He and He/H interfaces, which is consistent with the examination shown in Figure 4 of Paper I—the growth factors of seed perturbation around the interfaces of C+O/He and He/H in the progenitor model are prominent. Figure 7 shows results obtained from the model in which the perturbations at C+O/He and He/H interfaces are introduced.

We then present our simulation results for SC2. The results of the case with perturbation amplitude $\epsilon_0 = 50\%$ and $m = 8$ are shown in Figure 8, while the results of the case with perturbation amplitude $\epsilon_0 = 50\%$ and $m = 20$ are shown in Figure 9. For both cases, we take parameter $f = 5$. We see that RT fingers are developed and the matter mixing works: We obtain high velocity ^{56}Ni clumps. Cases with a small perturbation amplitude $\epsilon_0 = 10\%$ are also presented, and the results obtained from $m = 8$ and $m = 20$ are given. We show the results from the case of $\epsilon_0 = 50\%$, $m = 20$, and $f = 5$ as an example in Figure 10. Although we see some developed RT fingers, we confirm that the SC2 model with such small density perturbation cannot reproduce the matter mixing.

We further investigate the effect of radial coherent structure on the matter mixing

for SC2. This effect is dominated by the parameter f . A small number of f indicates a small length scale of density perturbation. Figure 11 shows the results of the simulation of $\epsilon_0 = 50\%$, $m = 20$, and $f = 1$ as an example. We cannot reproduce the matter mixing by this simulation model. As we can see from the density perturbation patterns in Figure 2, the perturbation mode of $f = 5$ provides the prominent coherent structure in the radial direction, and the matter mixing is obtained. The perturbation mode of $f = 1$ provides a far less coherent structure in the radial direction, so the matter mixing cannot be obtained.

We present our simulation results for SC3 at last. The density perturbation with 50% amplitude is considered in two simulation models, and $f = 1$ and $f = 5$ are taken, respectively, in each one. However, we do not find high velocity ^{56}Ni clumps in these simulation results. Figure 12 shows the results from the simulation model with $\epsilon_0 = 50\%$ and $f = 1$. As we see from the density perturbation patterns in Figure 2, the perturbation modes of SC3 do not provide any clear coherent structure in the radial direction. Thus, the matter mixing cannot be obtained.

We summarize our main results of the spherical explosion models: (1) The density perturbation amplitude is the most important parameter and RT instability dominates the matter mixing. RT fingers can be developed and the matter mixing can be reproduced by some simulation models with 50% of density perturbation. While 10% of density perturbation introduced in simulation models can generate RT fingers, but it is not enough to reproduce the matter mixing. (2) The synthesized ^{56}Ni and ^{44}Ti in the stellar interior can be effectively dug out because the radial coherent structures shown in perturbation patterns make the successful matter mixing in the CCSN explosion. (3) The matter mixing cannot be reproduced by the simulation model with the density perturbation introduced at the Si/C+O interface, but density perturbations at both the C+O/He and He/H interfaces can effectively achieve high velocity ^{56}Ni clumps. In other words, prominent density perturbations at large scales are successful for the matter mixing of a CCSN explosion. (4) The distribution of ^{56}Ni is roughly spherical in the simulation models where the matter mixing cannot be reproduced. If the simulation models are successful for the matter mixing, the distribution of ^{56}Ni is expected to be strongly anisotropic with prominent RT fingers. The properties of the heavy elements distribution shown in our simulation results indicate that SN 1987A may not favor spherical explosion models. (5) The distribution of ^{44}Ti follows that of ^{56}Ni . (6) Although we initially assume a spherical explosion in our simulation models, large density perturbations introduced in the progenitor may break down this spherical property. The set of initial conditions is important because it affects the evolution of the CCSN explosion.

We focus on ^{56}Ni velocity profiles in these spherical explosion models, and obtain high velocity ^{56}Ni clumps. We think that the matter mixing of SN 1987A can be qualitatively

reproduced by these models. We also further discuss two issues. First, the total mass of synthesized ^{56}Ni in our spherical simulation results is about two to three times of that of observational determinations (Shigeyama et al. 1988). Second, the explosion energy produced by our spherical simulations is about two times that of the observational fittings by Shigeyama et al. (1988) and Shigeyama & Nomoto (1990), although the explosion energy has a range of $(1 - 2) \times 10^{51}$ erg (Handy et al. 2014). We note that Kifonidis et al. (2006) produced the matter mixing in the CCSN with an explosion energy of 2×10^{51} erg, and Hammer et al. (2010) provided an explosion energy of 1.8×10^{51} erg in their 2D models. In order to examine the matter mixing of CCSN spherical explosions affected by the input energy, we reduce the input energy from 2.5×10^{51} to 1.7×10^{51} erg and re-perform one simulation model for SC1. Those results are shown in Figure 13. The explosion energy of 1.08×10^{51} erg calculated from this simulation model is consistent with the observational one given by Shigeyama et al. (1988). But the total synthesized ^{56}Ni mass is still larger than the observational one, and we do not obtain enough high velocity ^{56}Ni clumps. Therefore, it is necessary to perform simulation models of aspherical CCSN explosion to study matter mixing.

3.2. Aspherical Explosion

We present the results of aspherical explosion models in this subsection. First, we show the results of a bipolar model. Density distribution, distribution of the ^{56}Ni mass fraction, radial velocity of several elements, and line of sight velocity profiles of ^{56}Ni are shown in Figure 14. Due to this jet-like CCSN explosion, newly synthesized heavy elements in the stellar interior are pushed outside, mainly along the polar direction. Distribution of ^{56}Ni is roughly along the polar regions, and we see from the radial velocity profiles that the matter mixing works. We also successfully obtain high velocity ^{56}Ni clumps.

The results of the equatorially asymmetric explosion model are shown in Figure 15. Due to the asymmetric explosion across the equatorial plane, the density distribution and the distribution of ^{56}Ni are both equatorially asymmetric. The matter mixing is effective and high velocity ^{56}Ni clumps are obtained.

We also obtain the results of the combination model from the bipolar explosion and equatorial asymmetric explosion. In this global asymmetric case, the matter mixing is successfully produced. However, we overestimate masses of high velocity ^{56}Ni and ^{44}Ti when we introduce 50% of the density perturbation in the progenitor. In order to reproduce the proper high velocity ^{56}Ni clumps, we reduce the density perturbation amplitude from 50% to 25%. The resulting mass and velocity profiles of ^{56}Ni from the simulation model with the

reduced perturbation amplitude are consistent with the observational ones of SN 1987A. We also perform one simulation model of a global asymmetric case with 10% density perturbation amplitude. We confirm that the obtained high velocity ^{56}Ni clumps are not enough if only 10% of the density perturbation is introduced in the progenitor.

We summarize our main results for the matter mixing in an aspherical CCSN explosion: (1) Either bipolar explosion or equatorially asymmetric explosion can effectively reproduce high velocity ^{56}Ni clumps if we introduce 50% of the density perturbation in the progenitor. (2) We cannot obtain enough high velocity ^{56}Ni clumps from the simulation model with 10% of the density perturbation; at least 25% of the density perturbation is necessary to reproduce the observed matter mixing and high velocity ^{56}Ni clumps. (3) The distribution of ^{44}Ti follows that of ^{56}Ni . (4) The total ^{56}Ni mass and the mass of high velocity ^{56}Ni produced in aspherical explosion models roughly fit the observational values. However, the explosion energy is still overestimated compared to the number given by Shigeyama et al. (1988) and Shigeyama & Nomoto (1990).

In order to examine the matter mixing of the CCSN aspherical explosion affected by the input energy, we can reduce the input energy and re-perform simulation models. For example, we obtain our simulation results if the input energy is 2.0×10^{51} erg: the total ^{56}Ni mass is $0.07M_{\odot}$, high velocity ($> 3,000 \text{ km s}^{-1}$) ^{56}Ni mass is 6.5% of the total ^{56}Ni mass, and explosion energy is 1.43×10^{51} erg. The density distribution, distribution of ^{56}Ni mass fraction, radial velocity profiles of several elements, and line of sight velocity profiles of ^{56}Ni are shown in Figure 16. These results are consistent with the observational ones of SN 1987A. We regard this model (Asph+SC1p25m20** listed in Tables 1 and 2) as one of the most favorable simulation models in our work to explain the observational phenomena of the matter mixing in SN 1987A. The bipolar feature inferred from rotational CCSN explosion has been also explored by theoretical models (Nakamura et al. 2014).

4. Discussion

We introduce large density perturbations in the CCSN progenitor to investigate the matter mixing of the CCSN explosion. The consequent question is: What is the mechanism for the large density perturbation that occurs in stellar interiors? MLT is usually considered in the convection zones of the stellar interior (Kippenhahn & Weigert 1990). However, MLT is a local and spherically symmetric treatment in stellar models. Non-local and anisotropic convective mixing theories have been developed (Xiong 1977; Grossman et al. 1993; Xiong et al. 1997; Canuto & Dubovikov 1998; Deng et al. 2006; Li & Yang 2007; Hotta et al. 2014), but those treatments focus on the evolution of main-sequences stars. In addition, it seems

that the related overshooting in solar models and post-main-sequence star models (Tian et al. 2009; Li 2012; Zhang & Li 2012a,b) cannot strongly affect the matter mixing of CCSN explosion because the overshooting model is applied for the globally stable state of stars. However, the large density perturbation proposed in this paper is one requirement for the successful matter mixing of the CCSN explosion. Meakin & Arnett (2006) noticed that the spherically symmetric features in stellar interior can be broken as density perturbation is induced by turbulence within stellar convection zones. This kind of perturbation is related to carbon and oxygen shell burning. Analytic explorations and 3D simulations of turbulent convection have been performed, where turbulent entrainment and turbulent kinetic energy have been considered (Meakin & Arnett 2007a; Arnett et al. 2009). About 10% of density perturbation is obtained in convection zones as carbon and oxygen shell burning (Meakin & Arnett 2007b). Recently, Arnett & Meakin (2011a,b) found that violent dynamic eruptions occur in convective zones with simultaneous C, O, and Si shell burning of a CCSN progenitor star via 3D simulations. A realistic stellar model should provide aspherical properties from hydrodynamic instabilities and turbulence for CCSN explosion (Smith & Arnett 2014). Moreover, it has been found recently that the evolution of matter mixing is different between an BSG progenitor model and an RSG progenitor model (Wongwathanarat et al. 2015). In our 2D hydrodynamic simulation models, although 10% of density perturbation in the progenitor can produce RT fingers, 50% the of density perturbation is required in order to reproduce high velocity ^{56}Ni clumps. Our results provide additional clues to further analyze the turbulent convection of the CCSN explosion.

We have performed 2D hydrodynamic simulations to research of CCSN matter mixing in this work. Kane et al. (2000) pointed out that RT instability grows faster in 3D simulation models, and Hammer et al. (2010) reached a similar conclusion after comparing 2D and 3D simulation results. As Hammer et al. (2010) explained, heavy element clumps have toroidal topology in 2D simulations and bubble-sphere topology in 3D simulations, so these heavy element clumps experience less drag force in 3D simulations than in 2D ones. Thus, heavy element clumps can retain higher velocities in 3D models. If these physical processes mentioned above can really happen in CCSN explosions, we expect that less density perturbation should be introduced in 3D simulation models to reproduce high velocity ^{56}Ni clumps. However, it seems that Joggerst et al. (2010b) did not find qualitative differences of matter mixing efficiency between 2D and 3D simulations. One possible reason is that the interaction of the small RT fingers may reduce the final growth of RT instability, even if RT instability grows faster at the beginning of a CCSN explosion in 3D simulations. We can use 3D simulations with different density perturbation amplitudes to further investigate this CCSN matter mixing issue in the future.

We notice that RT fingers do not show a prominent feature at the early stage of CCSN

explosion. Couch & Ott (2013) proposed velocity perturbations in an angular direction at the Si/O interface of a progenitor. Their 3D simulations showed that this kind of perturbation can affect CCSN explosion. If we consider the neutrino-driven convection, the CCSN shock will be asymmetric around Fe/Si or Si/O boundaries. In fact, Kifonidis et al. (2006) claimed that the initial global deformation of the shock can trigger strong instability at the He/H boundary, which makes the global anisotropy of the inner ejecta. We find that large density perturbations placed at the Si/O interface may only provide and/or enhance aspherical features at the beginning of the CCSN explosion, but this does not give any direct effects on the matter mixing at the later time of the CCSN explosion. This discrepancy may be due to the application of different progenitors in different hydrodynamic simulation models. In our simulations, RT fingers are clearly identified after the shock propagates through the C+O/He interface. Giant RT fingers are developed quickly after the forward shock passes the He/H interface, and finally dominate at the late stage of CCSN explosion. During this later explosion process, we see a few small RT fingers merging into a large one, which was also mentioned by other previous works (Arnett et al. 1989; Kifonidis et al. 2003; Hammer et al. 2010; Ellinger et al. 2012). Moreover, when we successfully reproduce high velocity ^{56}Ni clumps, we clearly see the huge and prominent RT fingers with the length scale of about 2×10^{12} cm in these simulation models. However, the RT fingers with a length scale smaller than 1×10^{12} cm shown in some simulation models are short and weak, and we cannot reproduce high velocity ^{56}Ni clumps by these models.

The obtained total ^{56}Ni mass from spherical explosion models in this paper tends to be overestimated compared with that of SN 1987A. There are two possible reasons: First, if we reduce the input energy in spherical explosion models, the total ^{56}Ni mass can be reduced; second, a limited nuclear reaction network is included in the FLASH code and some isotopes of ^{56}Ni are neglected. Although a detailed discussion on the production of isotopes goes far beyond the scope of this paper, we attempt to examine the effect of neglecting isotopes on the production of ^{56}Ni by using a large nuclear reaction network. We perform a 1D hydrodynamic simulation of CCSN explosion without any perturbation using the same progenitor model mentioned in Section 2. The input energy is set to be 2.5×10^{51} erg. Then, explosive nucleosynthesis is calculated as a post-process using the large nuclear reaction network, including 464 nuclei. As a result, the following values are obtained: $M(^{56}\text{Ni}) = 0.14 M_{\odot}$, $M(^{57}\text{Ni}) = 0.01 M_{\odot}$, and $M(^{58}\text{Ni}) = 0.05 M_{\odot}$. On the other hand, $M(^{56}\text{Ni})$ obtained by 1D FLASH code is $0.21 M_{\odot}$. This indicates that the nuclear reaction network in the FLASH code may overestimate the mass of ^{56}Ni in a CCSN explosion. We present the detailed calculation process using the large nuclear reaction network in the Appendix.

We also notice that the masses of high velocity ^{56}Ni and ^{44}Ti clumps could be affected by the dimensionality in this paper. It is declared that 2D axisymmetric hydrodynamic

simulations have numerical problems due to the computational grid-geometry. Kifonidis et al. (2006) and Gawryszczak et al. (2010) mentioned that RT fingers may grow faster along the polar direction due to the discretization errors and the non-penetrating feature around the polar axis. Thus, the artificial axial jets are shown in axisymmetric simulation results. We have also observed these kinds of features in our simulation contours. We speculate that some extra high velocity clumps of ^{56}Ni and ^{44}Ti along the polar direction may be artificially produced by these axial jets. The productions of total ^{56}Ni and ^{44}Ti may be also affected by this geometric effect. In order to examine the axial jet effect, we perform a simple test. We consider the computational domain with angular direction from 15 degree to 165 degree and calculate total ^{56}Ni mass and high velocity ^{56}Ni clumps. We call this case “exclude15”. For comparison, we also consider the computational domain with angular direction from 30 degree to 150 degree and calculate the same quantities again. We call this case “exclude30”. Two simulation models-the spherical explosion model “SC1p50m20” and the bipolar explosion model “Bipo+C1p50m20”-are chosen. Line of sight velocity profiles and radial velocity profiles are shown in Figure 17. We see that the axial jet effect may produce artificial high velocity ^{56}Ni clumps. Bipolar aspherical explosion models may suffer from this effect more seriously than spherical explosion models. The related quantities are as follows: for the case of “exclude15” and “SC1p50m20”, total ^{56}Ni mass is $0.16 M_{\odot}$ and high velocity ($> 3,000 \text{ km s}^{-1}$) ^{56}Ni clumps have 5.5% of the total ^{56}Ni mass; for the case of “exclude30” and “SC1p50m20”, total ^{56}Ni mass is $0.15 M_{\odot}$ and high velocity ($> 3,000 \text{ km s}^{-1}$) ^{56}Ni clumps have 5.1% of the total ^{56}Ni mass; for the case of “exclude15” and “Bipo+C1p50m20”, total ^{56}Ni mass is $0.08 M_{\odot}$ and high velocity ($> 3,000 \text{ km s}^{-1}$) ^{56}Ni clumps have 8.5% of the total ^{56}Ni mass; for the case of “exclude30” and “Bipo+C1p50m20”, total ^{56}Ni mass is $0.06 M_{\odot}$ and high velocity ($> 3,000 \text{ km s}^{-1}$) ^{56}Ni clumps have 0.9% of the total ^{56}Ni mass. As a summary, the axial jet effect may only reduce a few percent of high velocity ^{56}Ni clumps in a spherical explosion model, but it may reduce at least 20% of high velocity ^{56}Ni clumps in a bipolar explosion model. 3D simulations are necessary for further quantitative analysis.

The observed line profiles of [Fe II] in SN 1987A are not symmetric and their peak is redshifted (Haas et al. 1990). The inner ring of SN 1987A is inclined at about 45° to the sky: the northern part of the ring is close to observers and the southern part of the ring is away from observers (Tziامتzis et al. 2011). The inner ejecta of SN 1987A is elongated and it is roughly in the same plane of the inner ring (Kjær et al. 2010). We calculate the line of sight velocity profiles of ^{56}Ni to different observational view angles. We define positive velocity and negative velocity in the line of sight velocity profiles as the redshifted velocity and blueshifted velocity, respectively. From our analysis of density contours and line of sight velocity profiles of ^{56}Ni , it looks like that the profile with observational view angle of 45° or 135° is morphologically close to the observational one. In particular, the peak shift is

dominated by the ratio of v_{up} and v_{down} when we consider equatorially asymmetric explosion models. A large value of the ratio leads to a strong peak shift. On the other hand, the density perturbation also affects the peak shift in equatorially asymmetric explosion models. We find that the large density perturbation tends to weaken the peak shift. Some fine tuning in simulation models is required to reproduce exactly the observational redshifted peak of line profile, although this is not the main scope in this paper. The results of our 2D simulations are helpful to understand the morphology of SN 1987A, but it is obvious that 3D simulations, which we plan to perform in the future, are more suitable to explain the reconstructed 3D features of SN 1987A (Kjær et al. 2010; Larsson et al. 2013).

Direct detections of emission lines from the decay of ^{44}Ti in two young supernova remnants have been reported. The mass of ^{44}Ti in SN 1987A was derived as $(3.1 \pm 0.8) \times 10^{-4} M_{\odot}$ (Grebenev et al. 2012) and the mass of ^{44}Ti in Cassiopeia A is about $1.6_{-0.3}^{+0.6} \times 10^{-4} M_{\odot}$ (Grefenstette et al. 2014). We also obtain the mass of ^{44}Ti in our simulation models. Our values obtained from the spherical explosion models are roughly comparable to the observational one, while the values obtained from the aspherical explosion models are larger than the observational one. Moreover, the ratios between the ^{56}Ni mass and ^{44}Ti mass in spherical explosion models are larger than those of aspherical models. If we overestimate the mass of ^{56}Ni in the spherical explosion models, the process of an α -rich freeze-out may enhance the production of ^{44}Ti (Woosley & Hoffman 1991; Nagataki 2000). The so-called mass-cut, which arbitrarily determines the location of the ejecta from the compact remnant may affect the mass of ^{44}Ti . However, it seems in Paper I that the differences of velocity profiles between the results with mass-cut and those without mass-cut are not significant. We also note that the overestimation of both ^{56}Ni and ^{44}Ti may be induced by the small nuclear reaction network in the FLASH code. Compared to the productions from spherical explosion models, it seems that those obtained from aspherical explosion models are more consistent with observational results. We confirm the speculation of Paper I that ^{44}Ti may be an indicator of explosion asphericity. However, we also realize that the production of ^{44}Ti and ^{56}Ni in the CCSN explosions is related to not only temperature and density, but also the electron fraction and detailed thermodynamic trajectories (Magkotsios et al. 2010). Postprocess calculations of the nucleosynthesis with a large nuclear reaction network are required. These complicated physical processes make some additional uncertainties to the ratio between ^{44}Ti and ^{56}Ni .

We can calculate radial velocities not only for the elements of H, ^{56}Ni , and ^{44}Ti , but also for the elements of ^4He , ^{12}C , ^{16}O , and ^{28}Si . The radial velocities of the elements in each simulation model are summarized in Table 3. If the simulation models of the spherical explosion with large density perturbation (50% amplitude) can produce high velocity ^{56}Ni and ^{44}Ti , the radial velocity profiles of ^{12}C , ^{16}O , and ^{28}Si also extend to a large velocity part. On the other hand, the simulation models of a spherical explosion with small density

perturbation (10% amplitude) cannot produce high velocity ^{56}Ni and ^{44}Ti , and it is also difficult to obtain more high velocity heavy elements of ^{12}C , ^{16}O , and ^{28}Si . In order to examine the effect of large density perturbation on the distributions of ^4He , ^{12}C , ^{16}O , and ^{28}Si , we plot the line of sight velocity profiles of these elements in Figure 18 (view angle 90 degree) and Figure 19 (view angle 45 degree). Three simulation models (SC1p50m20, SC1p10m20, and Asp+C1p50m20(*)) are considered. We see that ^{12}C , ^{16}O , and ^{28}Si are extended into the high velocity region in the spherical explosion model with 50% of density perturbation. Aspherical explosion with the view angle of 90 degree takes effects on the distribution of ^{12}C , ^{16}O , and ^{28}Si , so that these elements are concentrated in the center of line of sight velocity profiles. From the observational point of view, Larsson et al. (2013) have obtained [Si I]+[Fe II] line profiles of SN 1987A. The [Si I]+[Fe II] emission is close to the plane of the ring and the profile is north-south asymmetry that is partially due to dust absorption. The emission is concentrated in the velocity interval of 1500 – 3000 km s $^{-1}$. Tanaka et al. (2012) have measured the polarization features of [He I], [O I], [Ca II], and [Fe II] in type Ib/Ic SN 2009jf and SN 2009mi. In principle, this kind of spectral observation provides the opportunity for us to extract the velocity profiles of these elements. We expect that those velocity profiles calculated from our simulation models can be further examined by future observations and consequently provide additional hints to explore clumpy distributions and multi-dimensional geometries of CCSN explosions.

5. Summary

We perform 2D hydrodynamic simulations of a CCSN to explain the high velocity ^{56}Ni clumps of SN 1987A. The density perturbation with 50% amplitude is introduced in the progenitor model, such that the matter mixing can be reproduced in spherical explosion models. We take this large density perturbation to be one possible way to explain the final aspherical feature of a CCSN explosion indicated by the distributions of ^{56}Ni and ^{44}Ti . On the other hand, simulation models with 10% of density perturbation cannot reproduce high velocity ^{56}Ni clumps. The RT instability is efficient at both the C+O/He interface and He/H interface to reproduce high velocity ^{56}Ni clumps. The radial coherent structures shown in perturbation patterns are important to produce the matter mixing.

When we consider the case of aspherical explosion, at least 25% of density perturbation introduced in the progenitor is necessary to reproduce the high velocity ^{56}Ni clumps of SN 1987A. Either bipolar explosion or equatorially asymmetric explosion is effective for the explanation of observational matter mixing properties.

Explosion energy, total ^{56}Ni mass, total ^{44}Ti mass, and high velocity ($> 3,000$ km s $^{-1}$)

^{56}Ni mass have been obtained in each CCSN simulation model. The distribution of ^{44}Ti follows that of ^{56}Ni in all simulations models. After the comparison of our simulation results to the observations of SN 1987A, we note that one of the most favorable simulation models in this work is an aspherical one with the combination of bipolar explosion and equatorially asymmetric explosion, in which 25% of density perturbation is introduced at different composition interfaces of the CCSN progenitor.

As noted in Section 4, we have performed 2D simulations for the research of the matter mixing. However, 3D simulations may result in different matter mixing compared with 2D ones (Hammer et al. 2010). If we perform 3D simulations using the same progenitor, we expect that less density perturbations will be introduced to make the same matter mixing of SN 1987A. To obtain a more robust conclusion, we will perform 3D simulations for the matter mixing of SN 1987A in the future.

We are grateful to Dr. A., Wongwathanarat and T. Takiwaki for their useful discussion. The software used in this work was in part developed by the DOE NNSA-ASC OASCR Flash Center at the University of Chicago. Numerical computation in this work was carried out on SR16000 at the Yukawa Institute Computer Facility. Mao, J. is supported by the Hundred-Talent Program (Chinese Academy of Sciences). This work is also supported by the Ministry of Education, Culture, Sports, Science and Technology (MEXT: No. 23105709 and No. 26105521) and the Japan Society for the Promotion of Science (JSPS: No. 19104006, No. 23340069, No. 2503786, No. 25610056, No. 26287056, No. 26800159, No. 26800141 and No. 24.02022).

A. Production of ^{56}Ni and ^{44}Ti with a Large Nuclear Reaction Network

CCSN explosive nucleosynthesis has been comprehensively studied (Woosley & Arnett 1973; Hashimoto 1995) and applied for SN 1987A (Hashimoto et al. 1989; Woosley & Hoffman 1991). In this paper, we perform 2D hydrodynamic simulations using the FLASH code to study the matter mixing of CCSN explosion. As noted in Nagataki et al. (1997), some isotopes of ^{56}Ni should be included in the explosive nucleosynthesis. In order to clarify the effect of the small nuclear reaction network in the FLASH code to the production of ^{56}Ni and ^{44}Ti , we calculate the explosive nucleosynthesis using a large nuclear reaction network and a fiducial pure spherical explosion model.

We first perform a 1D hydrodynamic simulation of CCSN explosion using the same progenitor model and methods. The input energy of 2.5×10^{51} erg is adopted for a fiducial case. To calculate explosive nucleosynthesis as a post-process, we adopt the so-called tracer

particle method (Nagataki et al. 1997): 2,000 particles are distributed on the computational domain of the hydrodynamic simulation ($1.36 \times 10^8 \text{ cm} < r < 6 \times 10^9 \text{ cm}$, which covers up to the oxygen-rich layer), and mass and composition are assigned to each particle to reproduce the mass distribution and the composition of the progenitor model. Then, by using the results from the time evolution of the velocity field in Eulerian grids, particles are passively moved to obtain the time evolution of density and temperature. Using the initial composition and the time evolution of density and temperature, explosive nucleosynthesis is calculated for each ejected particle. We adopt a large nuclear reaction network including 464 nuclei (up to ^{94}Kr), which was used in Ono et al. (2009). It should be noted that the innermost region ($r = 1.36 \times 10^8 \text{ cm}$) is slightly neutron-rich (electron fraction $Y_e \sim 0.485$) and the production of neutron-rich isotopes, ^{57}Ni and ^{58}Ni , is expected. As a result, we obtain the following values: $M(^{56}\text{Ni}) = 1.4 \times 10^{-1} M_\odot$, $M(^{57}\text{Ni}) = 1.0 \times 10^{-2} M_\odot$, $M(^{58}\text{Ni}) = 5.4 \times 10^{-2} M_\odot$, and $M(^{44}\text{Ti}) = 1.0 \times 10^{-4} M_\odot$. The masses of ^{56}Ni and ^{44}Ti estimated by the FLASH code are $2.1 \times 10^{-1} M_\odot$ and $3.0 \times 10^{-4} M_\odot$ respectively. Thus, the masses of ^{56}Ni and ^{44}Ti calculated by the FLASH code are overestimated by a factor of 0.7 and a factor of 3, respectively, compared with those calculated by the large nuclear reaction network. Because the amount of ^{44}Ti is much less than that of ^{56}Ni , the overestimation of ^{44}Ti due to neglecting other elements is more severe than that of ^{56}Ni .

REFERENCES

- Ahmad, I., Greene, J. P., Moore, E. F., Ghelberg, S., Ofan, A., Paul, M., & Kutschera, W. 2006, *Phys. Rev. C.*, 74, 065803
- Arnett, W. D. 1994, *ApJ*, 427, 932
- Arnett, W. D., Fryxell, B., & Müller, E. 1989, *ApJ*, 341, L63
- Arnett, W. D., Meakin, C., & Young, P. A. 2009, *ApJ*, 690, 1715
- Arnett, W. D., & Meakin, C. 2011a, *ApJ*, 733, 78
- Arnett, W. D., & Meakin, C. 2011b, *ApJ*, 741, 33
- Bazan, G., & Arnett, W. D. 1994, *ApJ*, 433, L41
- Bazan, G., & Arnett, W. D. 1998, *ApJ*, 496, L316
- Benz, W., & Thielemann, F.-K. 1990, *ApJ*, 348, L17
- Blondin, J. M., Mezzacappa, A., & DeMarino, C. 2003, *ApJ*, 584, 971

- Bruenn, S. W., Mezzacappa, A., Hix, W. R. et al. 2013, ApJ, 767, L6
- Burrows, A., Hayes, J., & Fryxell, B. A. 1995, ApJ, 450, 830
- Burrows, A., Dessart, L., Livne, E., Ott, C. D., & Murphy, J. 2007, ApJ, 664, 416
- Burrows, A. 2013, RvMP, 85, 245
- Canuto, V. M., & Dubovikov, M. 1998, ApJ, 493, 834
- Cawthorne, T. V., & Cobb, W. K. 1990, ApJ, 350, 536
- Chevalier, R. A. 1976, ApJ, 207, 872
- Coburn, W., & Boggs, S. E. 2003, Nature, 423, 415
- Couch, S. M., & Ott, C. D. 2013, ApJ, 778, L7
- Couch, S. M., & Ott, C. D. 2014, ApJ, 799, 5
- Decin, L., Cox, N. L. J., Royer, P., et al. 2012, A&A, 548, A113
- Deng, L., Xiong, D. R., & Chan, K. L. 2006, ApJ, 643, 426
- Dotani, T., Hayashida, K., Inoue, H., et al. 1987, Nature, 330, 230
- Dwek, E., Arendt, R. G., Bouchet, P., et al. 2010, ApJ, 722, 425
- Ebisuzaki, T., Shigeyama, T., & Nomoto, K. 1989, ApJ, 344, L65
- Ellinger, C. I., Young, P. A., Fryer, C. L., & Rockefeller, G. 2012, ApJ, 755, 160
- Fransson, C., & Kozma, C. 1993, ApJ, 408, L25
- Fryxell, B., Olson, K., Picker, P., et al. 2000, ApJS, 131, 273
- Gawryszczak, A., Guzman, J., Plewa, T. & Kifonidis, K. 2010, A&A, 521, A38
- Grebenev, S. A., Lutovinov, A. A., Tsygankov, S. S. & Winkler, C. 2012, ApJ, 490, 373
- Grefenstette, B. W., Harrison, F. A., Boggs, S. E., et al. 2014, Nature, 506, 339
- Gröningsson, P., Fransson, C., Leibundgut, B., Lundqvist, P., Challis, P., Chevalier, R. A., & Spyromilio, J. A&A, 492, 481
- Grossman, S. A., Narayan, R., & Arnett, D. 1993, ApJ, 407, 284

- Haas, M. R., Erickson, F. A., Lord, S. D., et al. 1990, *ApJ*, 360, 257
- Hammer, N. J., Plewa, T., & Müller, E. 2010, *ApJ*, 714, 1371
- Handy, T., Janka, H.-T., & Odrzywolek, A. 2014, *ApJ*, 783, 125
- Hanke, F., Müller, B., Wongwathanarat, A., Marek, A., & Janka, H.-T. 2013, *ApJ*, 770, 66
- Hashimoto, M., Nomoto, K., & Shigeyama, T. 1989, *A&A*, 210, L8
- Hashimoto, M. 1995, *Progress of Theoretical Physics*, 94, 663
- Hanuschik, R., Thimm, G., & Dachs, J. 1988, *MNRAS*, 234, 41
- Herant, M., & Benz, W. 1991, *ApJ*, 370, L81
- Herant, M., & Benz, W. 1992, *ApJ*, 387, 294
- Herant, M., Benz, W., Hix, W. R., Fryer, C. L., & Colgate, S. A. 1994, *ApJ*, 435, 339
- Hotta, H., Rempel, M., & Yokoyama, T. 2014, *ApJ*, 786, 24
- Hungerford, A. L., Fryer, C. L., & Warren, M. S. 2003, *ApJ*, 594, 390
- Hungerford, A. L., Fryer, C. L., & Rockefeller, G. 2005, *ApJ*, 635, 487
- Janka, H.-T., & Müller, E. 1995, *ApJ*, 448, L109
- Janka, H.-T. 2012, *Annual Review of Nuclear and Particle Science*, 62, 407
- Jerkstrand, A., Fransson, C., & Kozma, C. 2011, *A&A*, 530, A45
- Joggerst, C. C., Woosley, H., & Heger, A. 2009, *ApJ*, 693, 1780
- Joggerst, C. C., Almgren, A., Bell, J., Heger, A., Whalen, D., & Woosley, S. E., 2010a, *ApJ*, 709, 11
- Joggerst, C. C., Almgren, A., & Woosley, S. E., 2010b, *ApJ*, 723, 353
- Kane J., Arnett, D., Remington, B. A., Glendinning, S. G., Bazán, G., Müller, E., Fryxell, B. A., & Teyssier, R. 2000, *ApJ*, 528, 989
- Kifonidis, K., Plewa, T., Janka, H.-T., & Müller, E. 2003, *A&A*, 408, 621
- Kifonidis, K., Plewa, T., Scheck, L., Janka, H.-T., & Müller, E. 2006, *A&A*, 453, 661

- Kjær, K., Leibundgut, B., Fransson, C., Jerkstrand, A., & Spyromilio, J. 2010, *A&A*, 517, A51
- Kotake K., Sawai, H., Yamada, S., & Sato, K. 2004, *ApJ*, 608, 391
- Kotake K., Sato, K., & Takahashi, K. 2006, *Rep. Prog. Phys.* 69, 971
- Kotake K., Takiwaki, T., Suwa, Y., Iwakami, N. W., Kawagoe, S., Masada, Y., & Fujimoto, S. 2012, *Adv. Astron.* 428757
- Kuroda, T., Kotake, K., & Takiwaki, T. 2012, *ApJ*, 755, 11
- Larsson, J., Fransson, C., Kjaer, K., et al. 2013, *ApJ*, 768, 89
- Leising, M. D., & Share, G. H. 1990, *ApJ*, 357, 638
- Li, Y., & Yang, J. Y. 2007, *MNRAS*, 375, 388
- Li, Y. 2012, *ApJ*, 756, 37
- Kippenhahn, R., & Weigert, A. 1990, *Stellar Structure and Evolution* (Berlin: Springer)
- Magkotsios, G., Timmes, F. X., Hungerford, A. L., Fryer, C. L., Young, P. A., & Wiescher, M. 2010, *ApJS*, 191, 66
- Matz, S. M., Share, G. H., Leising, M. D., Chupp, E. L., Vestrand, W. T., Purcell, W. R., Strickman, M. S., & Reppin, C. 1988, *Nature*, 331, 416
- Meakin, C. A. & Arnett, W. D. 2006, *ApJ*, 637, L53
- Meakin, C. A. & Arnett, W. D. 2007a, *ApJ*, 667, 448
- Meakin, C. A. & Arnett, W. D. 2007b, *ApJ*, 665, 690
- Montarges, M., Kervella, P., Perrin, G., Ohnaka, K., Chiavassa, A., Ridgway, S. T., & Lacour, S. 2014, *A&A*, 572, A17
- Müller, E., Fryxell, B., & Arnett, W. D. 1991, *A&A*, 251, 505
- Müller, B., Janka, H.-T., & Heger, A. 2012, *ApJ*, 761, 72
- Murphy, J. W., & Meakin, C. 2011, *ApJ*, 742, 74
- Murphy, J. W., Dolence, J. C., & Burrows, A. 2013, *ApJ*, 771, 52
- Nagataki, S., Hashimoto, M., Sato, K., & Yamada, S. 1997, *ApJ*, 486, 1026

- Nagataki, S., Shimizu, T. M., & Sato, K. 1998, *ApJ*, 495, 413
- Nagataki, S. 2000, *ApJS*, 127, 141
- Nakamura, K., Kuroda, T., Takiwaki, T., & Kotake, K. 2014, *ApJ*, 793, 45
- Nomoto, K., & Hashimoto, M. 1988, *Phys. Rep.*, 163, 13
- Nordhaus, J., Burrows, A., Almgren, A., & Bell, J. 2010, *ApJ*, 720, 694
- Ono, M., Hashimoto, M, Fujimoto, S., Kotake, K., & Yamada, S. 2009, *Prog. Theor. Phys.* 122, 755
- Ono, M., Nagataki, S., Ito, H., Lee, S.-H., Mao, J., Hashimoto, M., & Tolstov, A. 2013, *ApJ*, 773, 161
- Ott, C. D., Abdikamalov, E., Mosta, P., et al. 2013, *ApJ*, 768, 115
- Sawai, H., Kotaki, K., & Yamada, S. 2005, *ApJ*, 631, 446
- Sawai, H., Yamada, S., & Suzuki, H. 2013, *ApJ*, 770, L19
- Shigeyama, T., Nomoto, K., Hashimoto, M., & Sugimoto, D. 1987, *Nature*, 328, 320
- Shigeyama, T., Nomoto, K., & Hashimoto, M. 1988, *A&A*, 196, 141
- Shigeyama, T., & Nomoto, K. 1990, *ApJ*, 360, 242
- Sinnott, B., Welch, D. L., Rest, A., Sutherland, P. G., & Bergmann, M. 2013, *ApJ*, 767, 45
- Smith, N. 2007, *AJ*, 133, 1034
- Smith, N., & Arnett, W. D. 2014, *ApJ*, 785, 82
- Spyromilio, J., Meikle, W. P. S., & Allen, D. A. 1990, *MNRAS*, 242, 669
- Steffen, M. 1990, *A&A*, 239, 443
- Sunyaev, R. A., Kaniovsky, A., Efremov, V., et al. 1987, *Nature*, 330, 227
- Suwa, Y., Kotake, K., Takiwaki, T., Whitehouse, S. C., Liebendörfer, M., & Sato, K. *PASJ*, 62, L49
- Suwa, Y., Kotake, K., Takiwaki, T., Liebendörfer, M., & Sato, K. 2011, *ApJ*, 738, 165
- Takiwaki, T., Kotaki, K., & Sato, K. 2009, *ApJ*, 691, 1360

- Takiwaki, T., Kotaki, K., & Sato, K. 2014, *ApJ*, 786, 83
- Tanaka, M., Kawabata, K. S., Hattori, T., et al. 2012, *ApJ*, 754, 63
- Tian, C.-L., Deng, L.-C., & Chan, K.-L. 2009, *MNRAS*, 398, 1011
- Tziamtzis, A., Lundqvist, P., Gröningsson, P., & Nasoudi-Shoar, S. 2011, *A&A*, 527, A35
- Utrobin, V. P., Chugai, N. N., & Andronova, A. A. 1995, *A&A*, 295, 129
- Wongwathanarat, A., Janka, H.-T., & Müller, E. 2013, *A&A*, 552, A126
- Viallet, M., Meakin, C., Arnett, D., & Mocák, M. 2013, *ApJ*, 769, 1
- Wongwathanarat, A., & Müller, E., & Janka, H.-T. 2015, *A&A*, 577, A48
- Woosley, S. E., & Arnett, W. D. 1973, *ApJS*, 26, 231
- Woosley, S. E., & Hoffman, R. D. 1991, *ApJ*, 368, L31
- Xiong, D. R. 1977, *Acta Astron. Sinica*, 18, 86
- Xiong, D. R., Cheng, Q. L., & Deng, L. 1997, *ApJS*, 108, 529
- Yamada, S., & Sato, K. 1991, *ApJ*, 382, 594
- Zhang, Q.-S., & Li, Y. 2012a, *ApJ*, 746, 50
- Zhang, Q.-S., & Li, Y. 2012b, *ApJ*, 750, 11

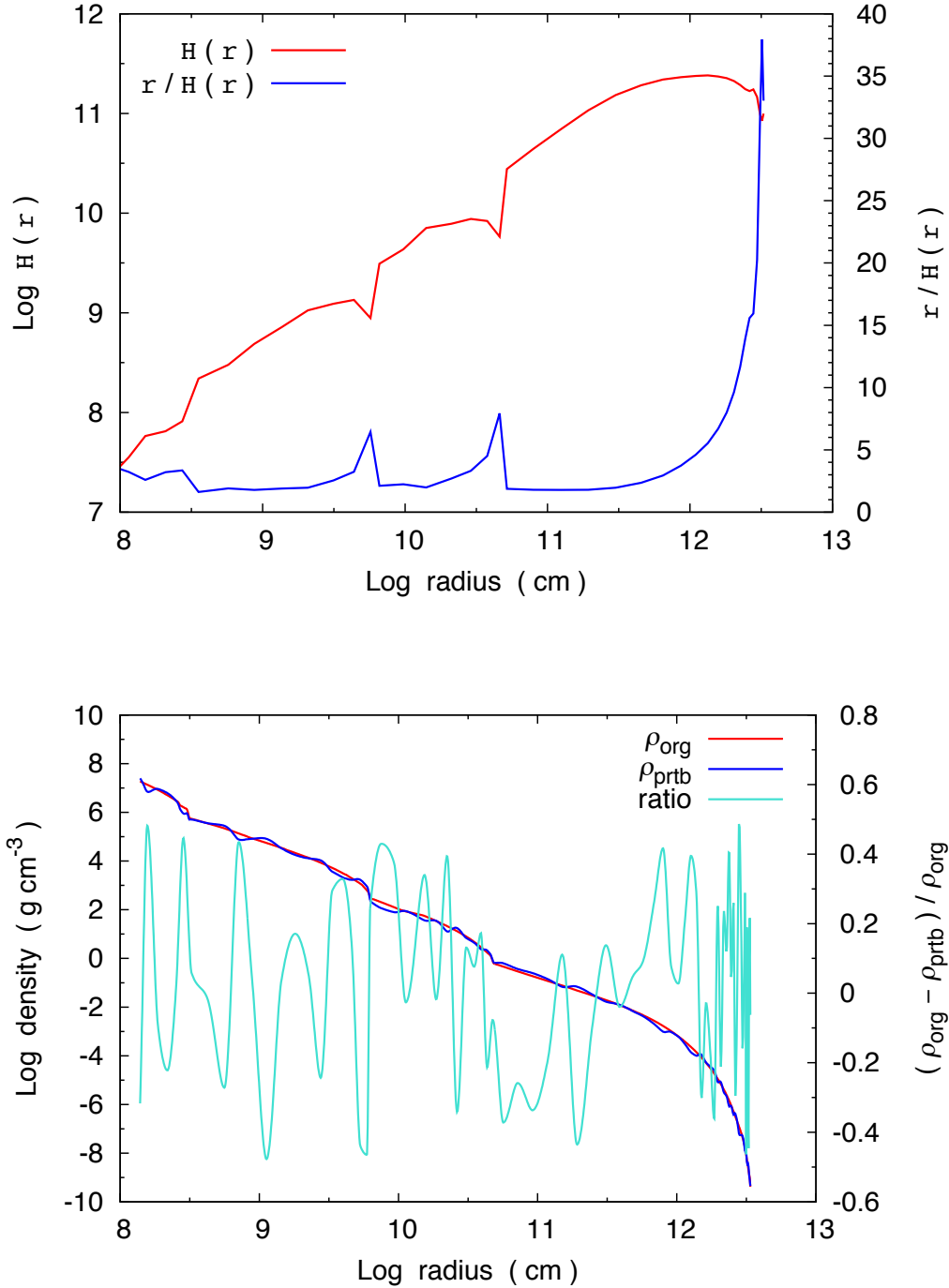


Fig. 1.— Upper panel: density scale height $H(r)$ and $r/H(r)$ of the progenitor model as a function of radius; lower panel: profiles of density and density perturbation in the progenitor model. Distributions of original density, perturbative density, and perturbation amplitude are denoted by red, blue, and cyan lines, respectively. Perturbation amplitude is randomly distributed in the radial direction and the maximum value is 50%. We take this perturbation mode from the case of SC3 ($\epsilon_0 = 0.5$ and $f = 1$).

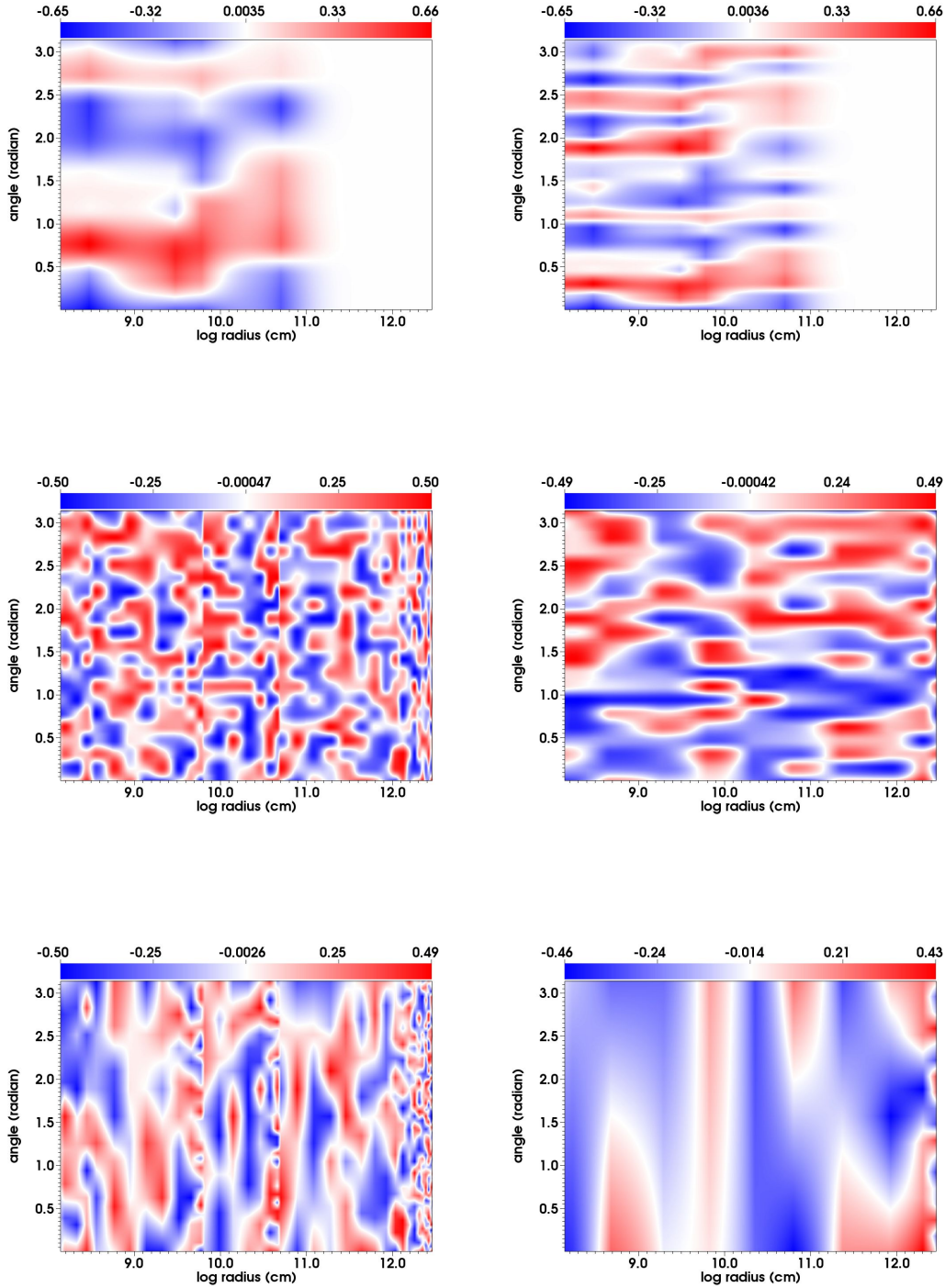


Fig. 2.— Distributions of density perturbation in the r - θ plane. The ranges of r and θ are $1.4 \times 10^8 \text{ cm} < r < 3.4 \times 10^{12} \text{ cm}$ and $0 < \theta < \pi$, respectively, and the color bar in the top of each panel denotes the amplitude range of perturbation. upper left: perturbation mode of SC1 ($m=8$); Upper right: perturbation mode of SC1 ($m=20$); middle left: perturbation mode of SC2 ($m = 20$ and $f = 1$); middle right: perturbation mode of SC2 ($m = 20$ and $f = 5$); lower left: perturbation mode of SC3 ($m = 20$ and $f = 1$); lower right: perturbation mode of SC3 ($m = 20$ and $f = 5$). We note four critical radii: $3 \times 10^8 \text{ cm}$ at Si/C+O interface, $3 \times 10^9 \text{ cm}$ at oxygen shell burning position, $6 \times 10^9 \text{ cm}$ at C+O/He interface, and $5 \times 10^{10} \text{ cm}$ at He/H interface. Only the models with coherent-structured perturbation in the radial direction can reproduce high velocity clumps of ^{56}Ni (see upper left, upper right, and middle right panels).

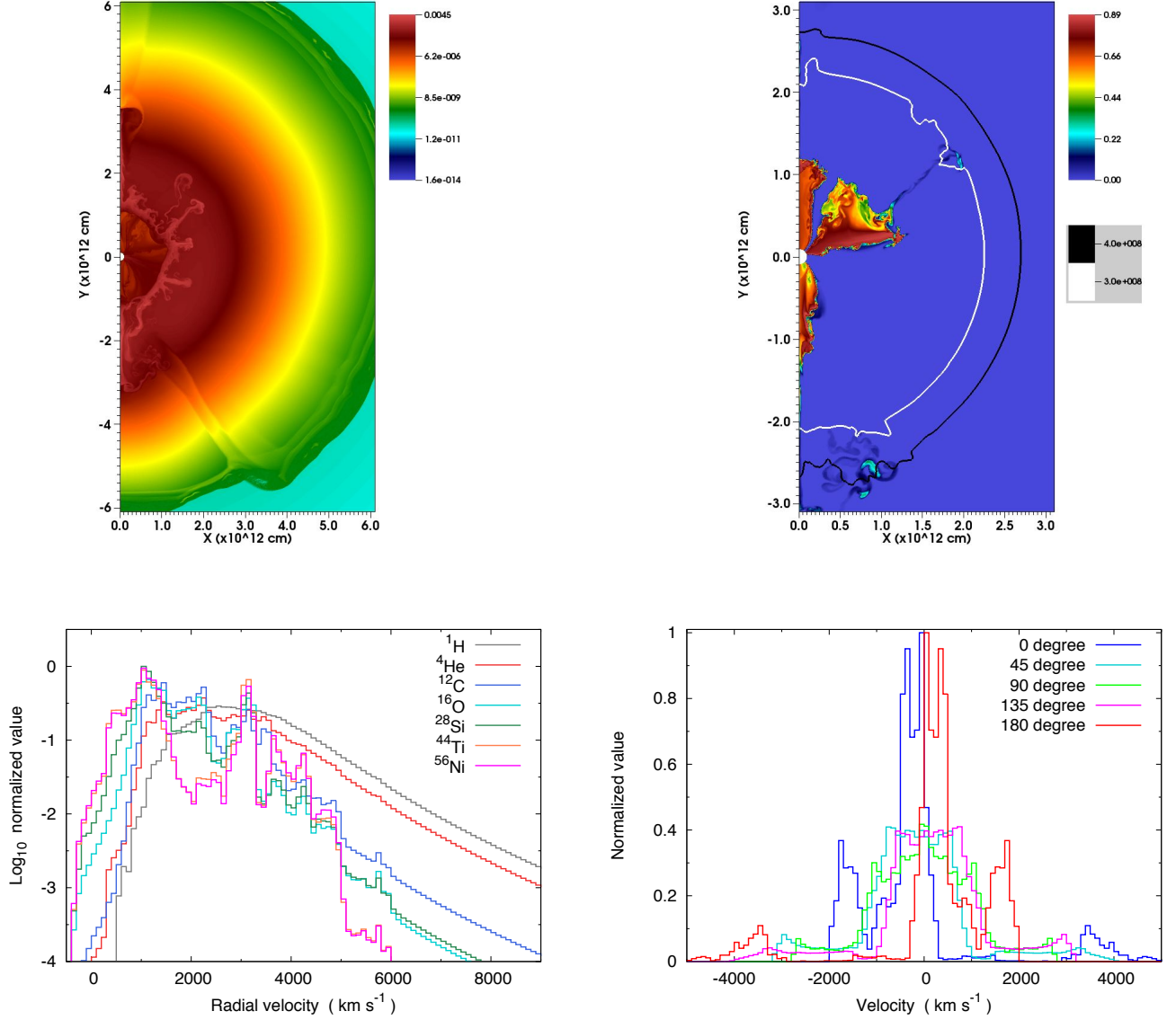


Fig. 3.— Results obtained from the model SC1p50m8. Upper left: final density distribution; upper right: final distribution of ^{56}Ni mass fraction. The white and black lines indicate the contours of radial velocities of $3,000 \text{ km s}^{-1}$ and $4,000 \text{ km s}^{-1}$, respectively; Lower left: radial velocity profile; lower right: line of sight velocity profile of ^{56}Ni with different observational view angles. For each lower panel, the velocity bin is 100 km s^{-1} , numbers of $\Delta M/M$ are normalized by their maximum value, where ΔM is the mass in the velocity range of $v \sim v + \Delta v$; and M is the total mass.

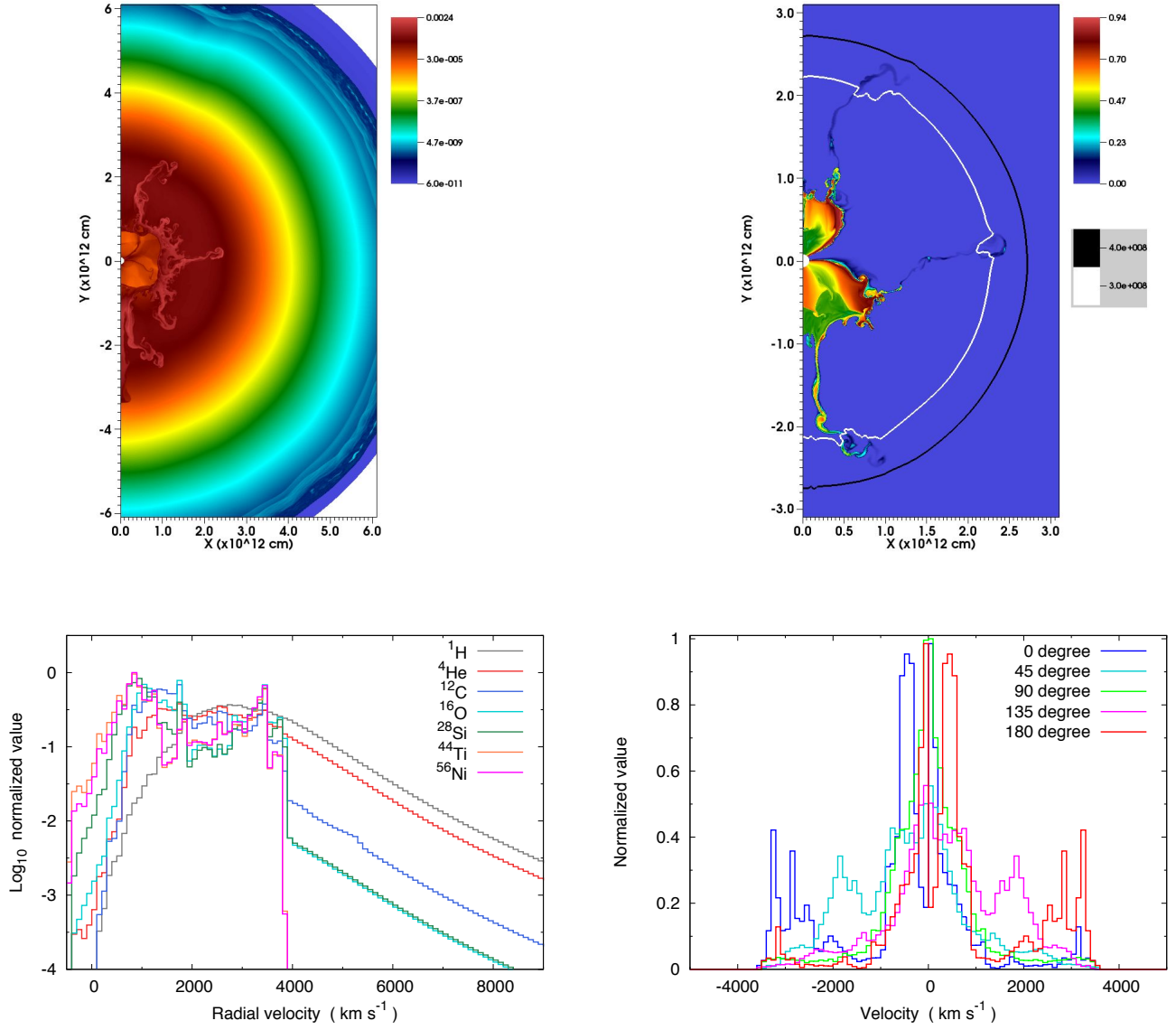


Fig. 4.— Results obtained from the model SC1p50m8 with a different set of random numbers. Panel descriptions are the same as those in Figure 3.

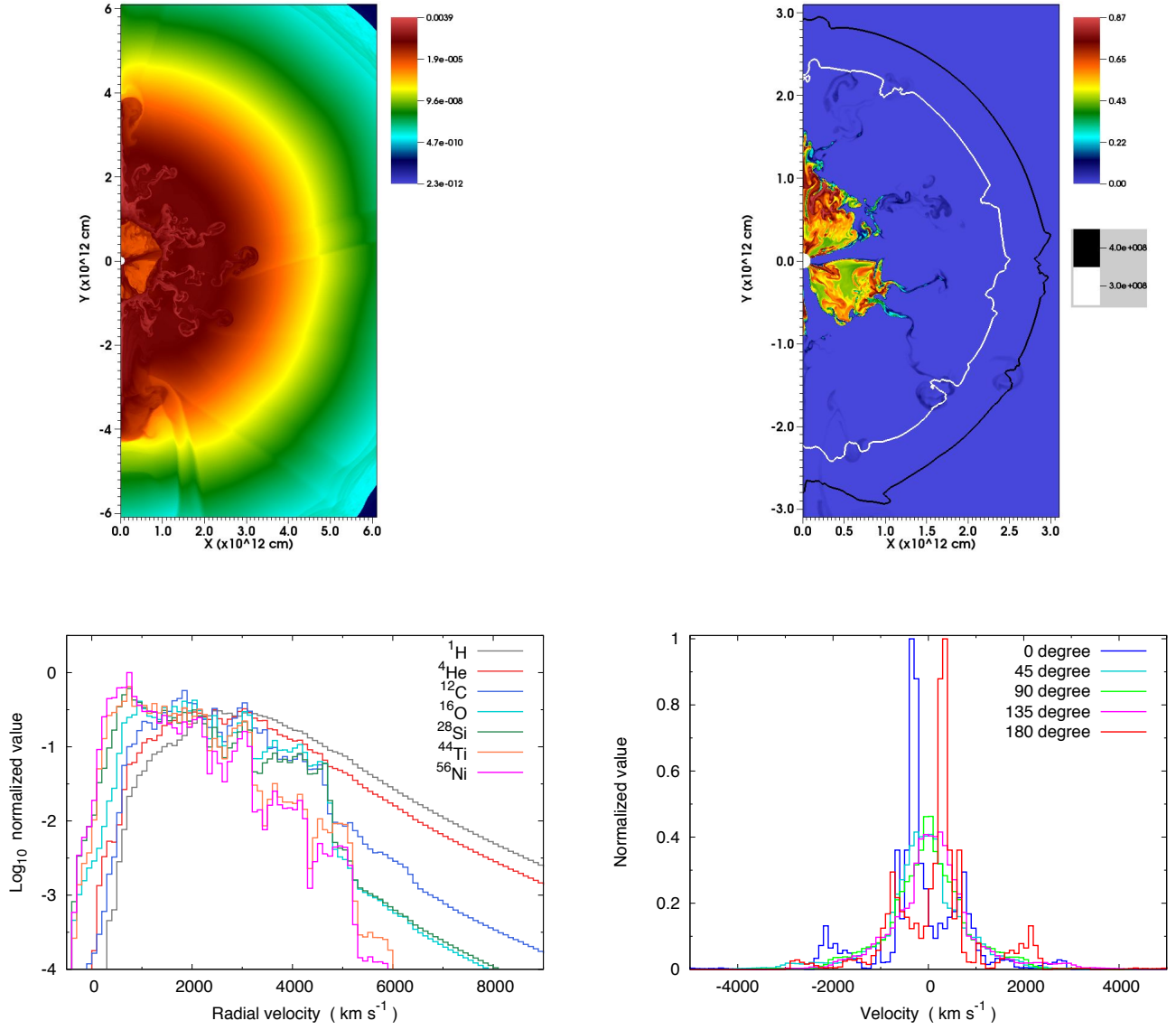


Fig. 5.— Results obtained from the model SC1p50m20. Panel descriptions are the same as those in Figure 3.

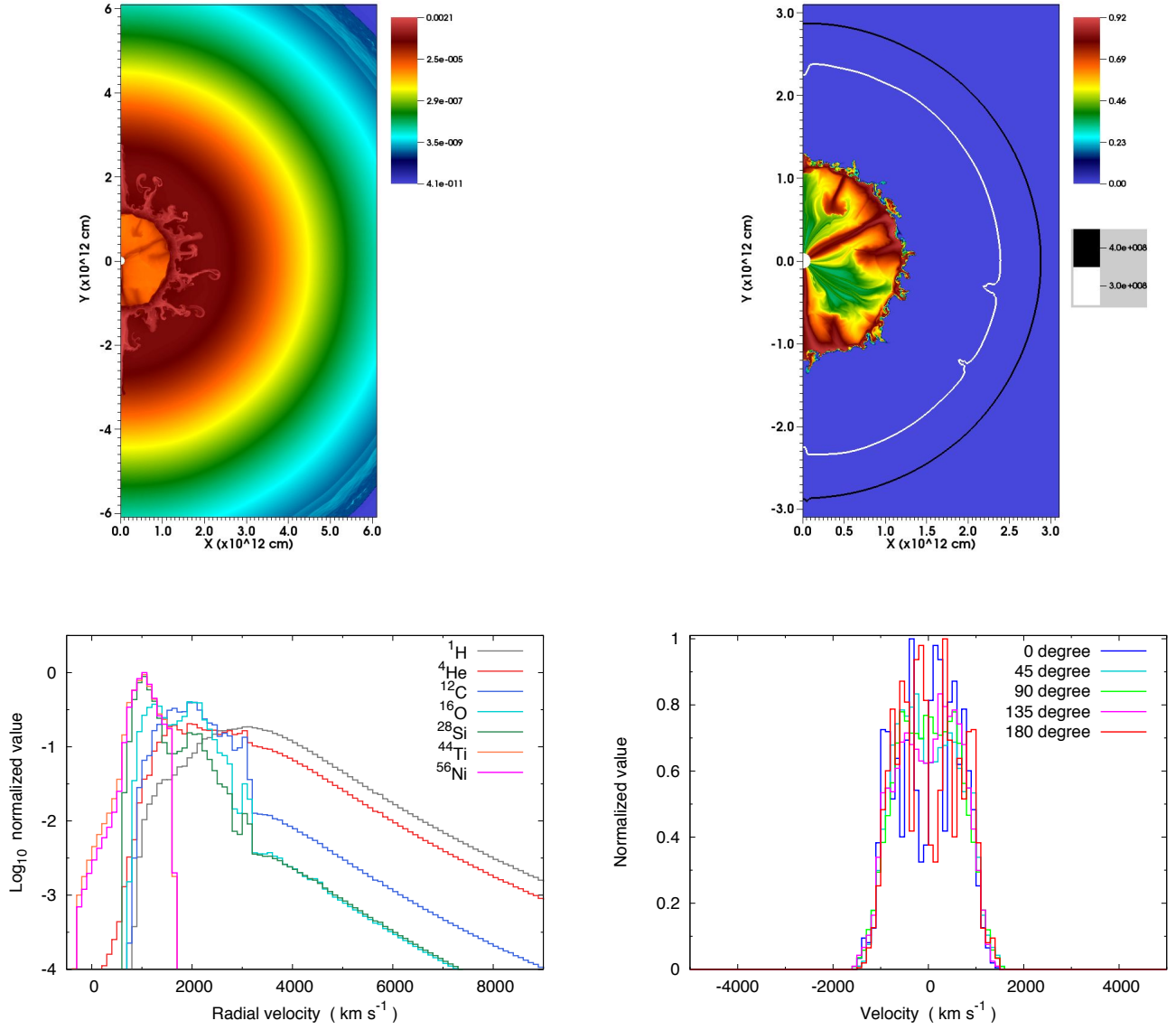


Fig. 6.— Results obtained from the model SC1p10m20. Panel descriptions are the same as those in Figure 3.

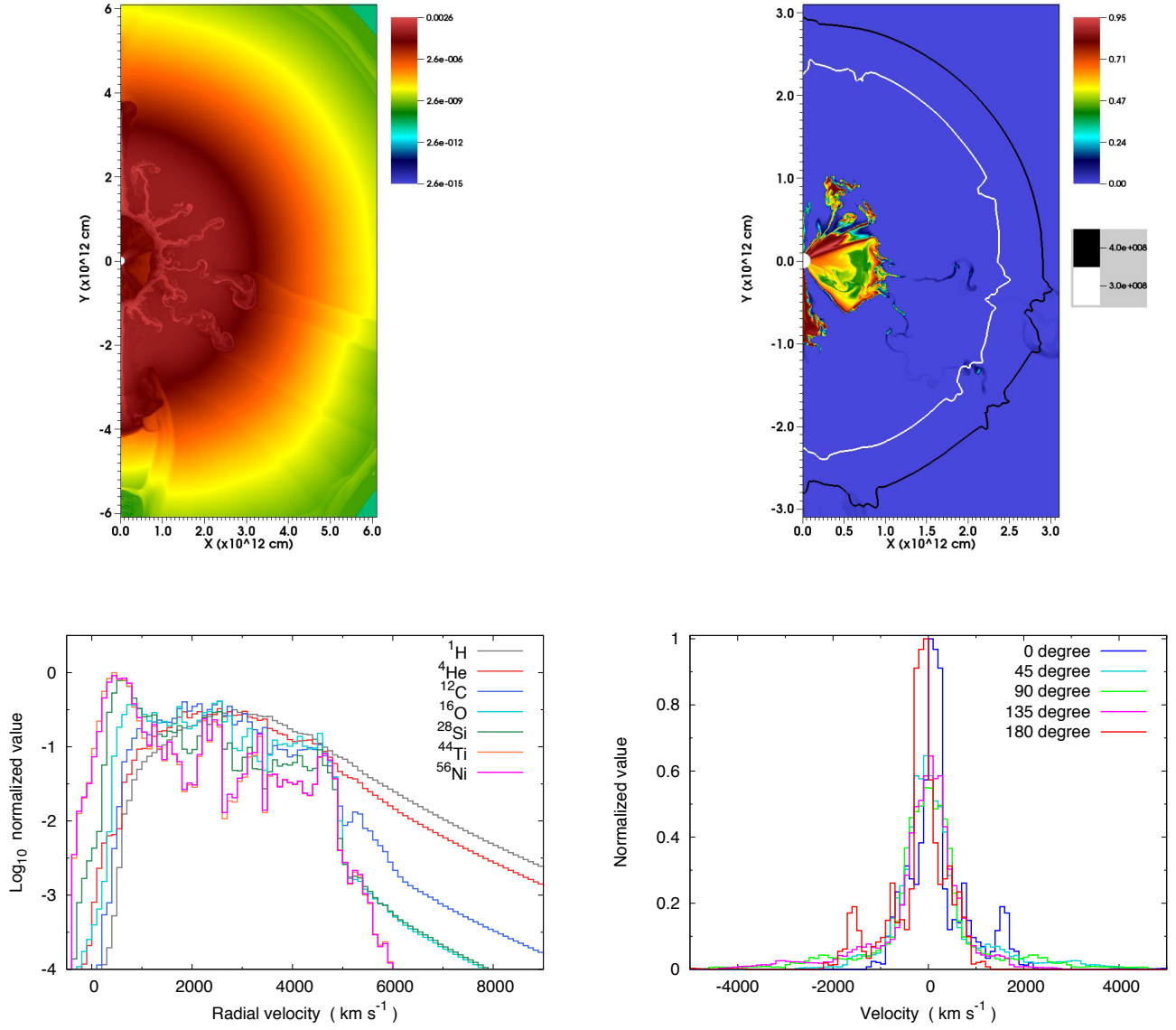


Fig. 7.— Results obtained from the model SC1C+O/He/H. Panel descriptions are the same as those in Figure 3.

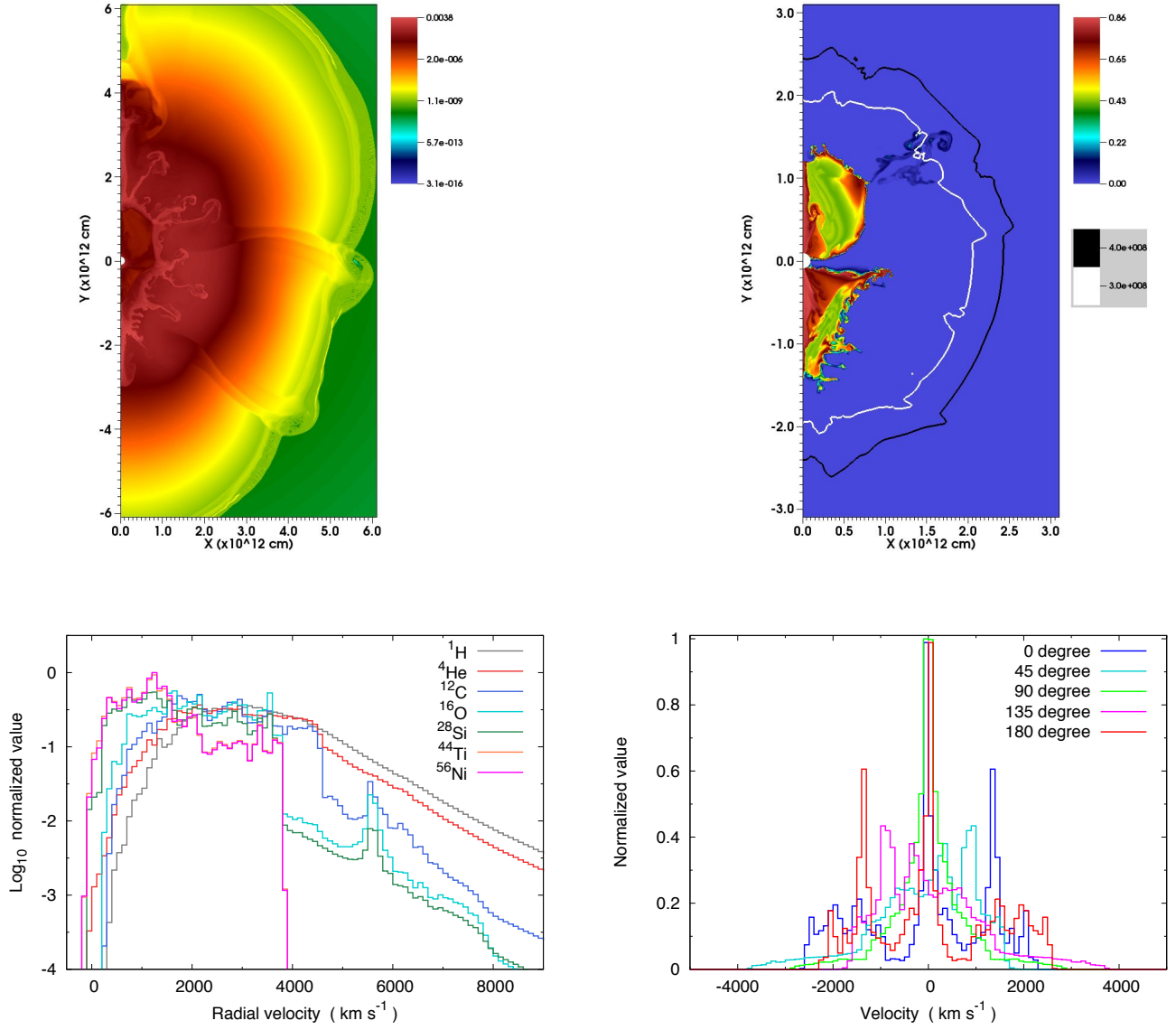


Fig. 8.— Results obtained from the model SC2p50m8f5. Panel descriptions are the same as those in Figure 3.

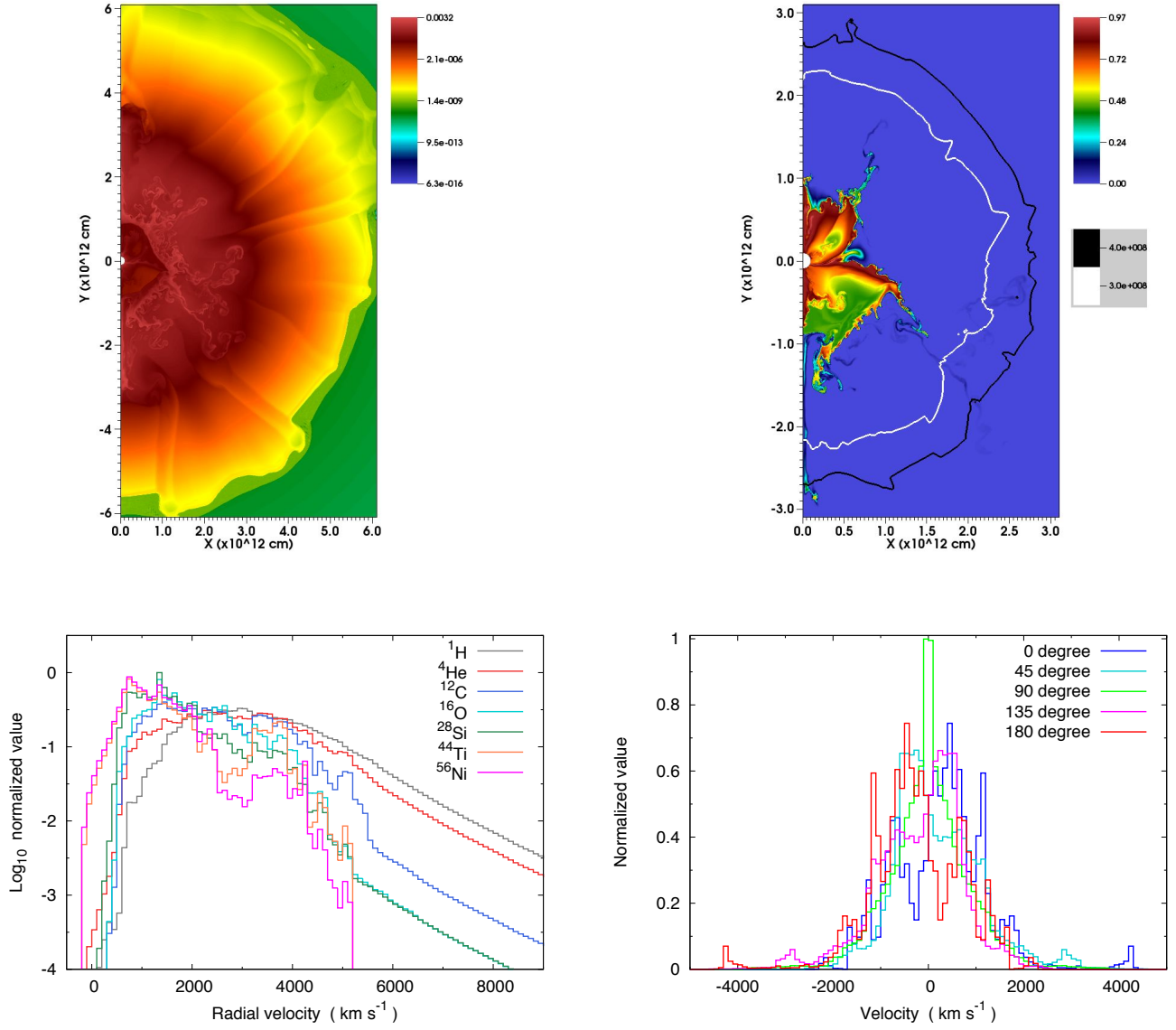


Fig. 9.— Results obtained from the model SC2p50m20f5. Panel descriptions are the same as those in Figure 3.

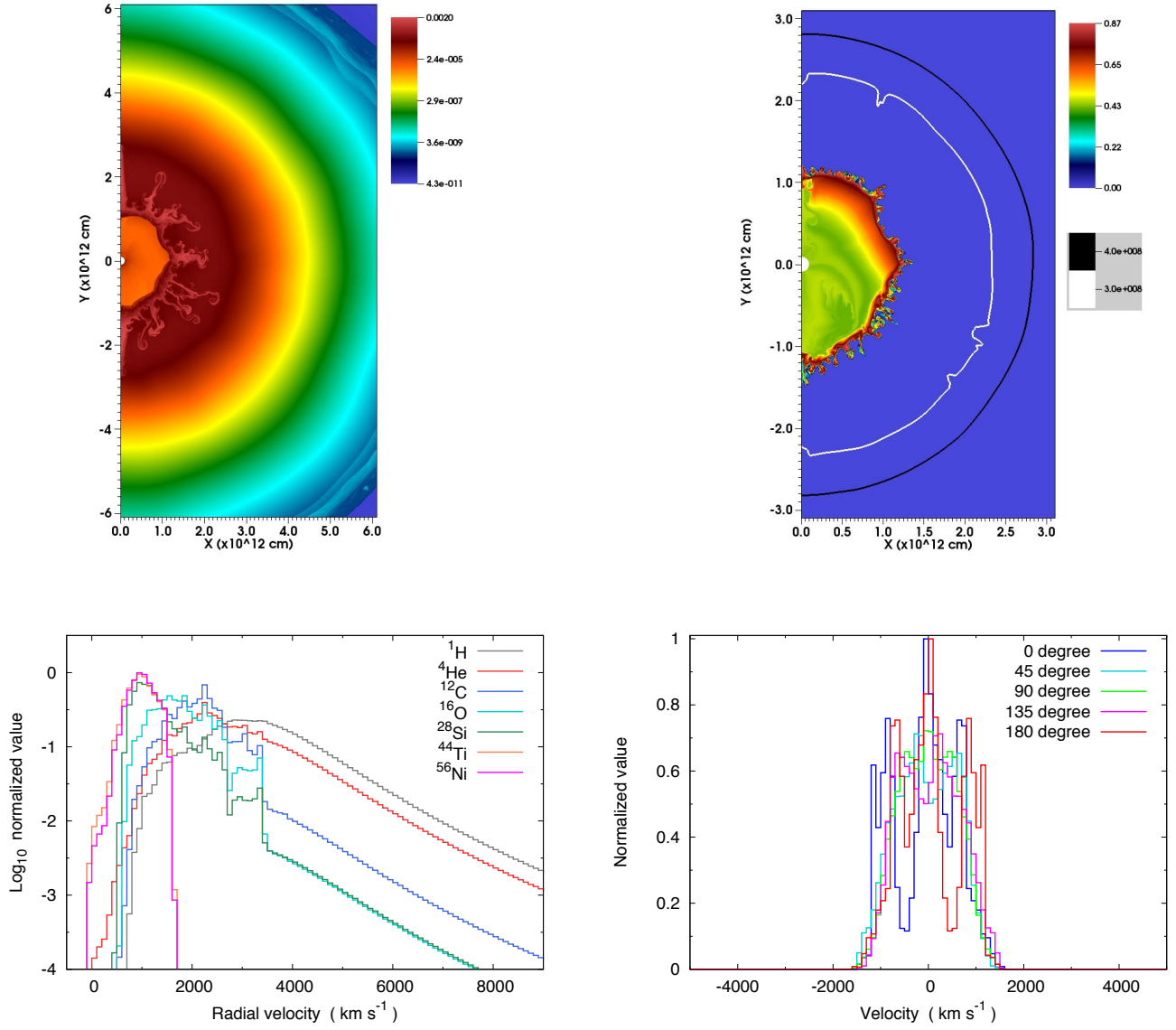


Fig. 10.— Results obtained from the model SC2p10m20f5. Panel descriptions are the same as those in Figure 3.

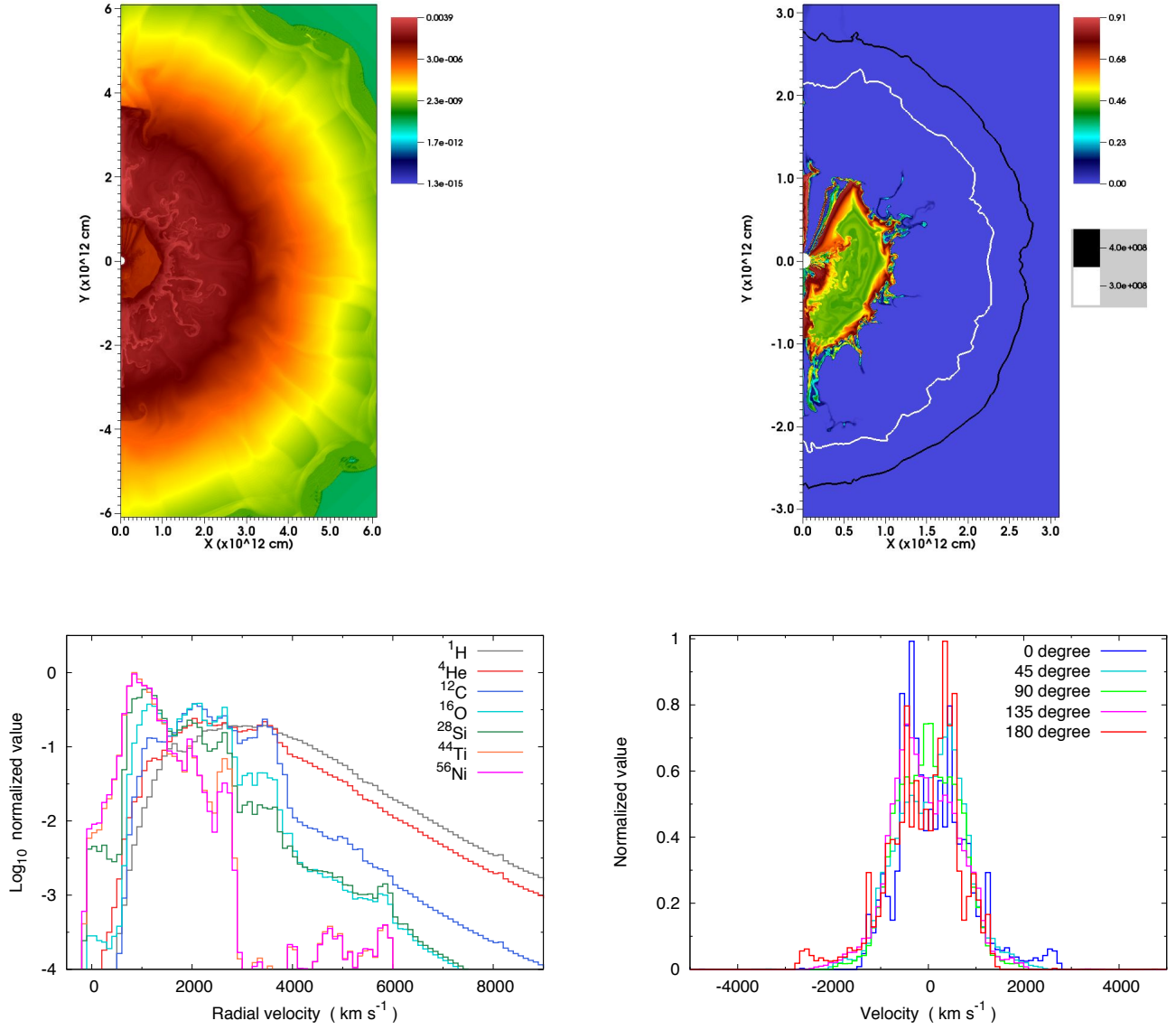


Fig. 11.— Results obtained from the model SC2p50m20f1. Panel descriptions are the same as those in Figure 3.

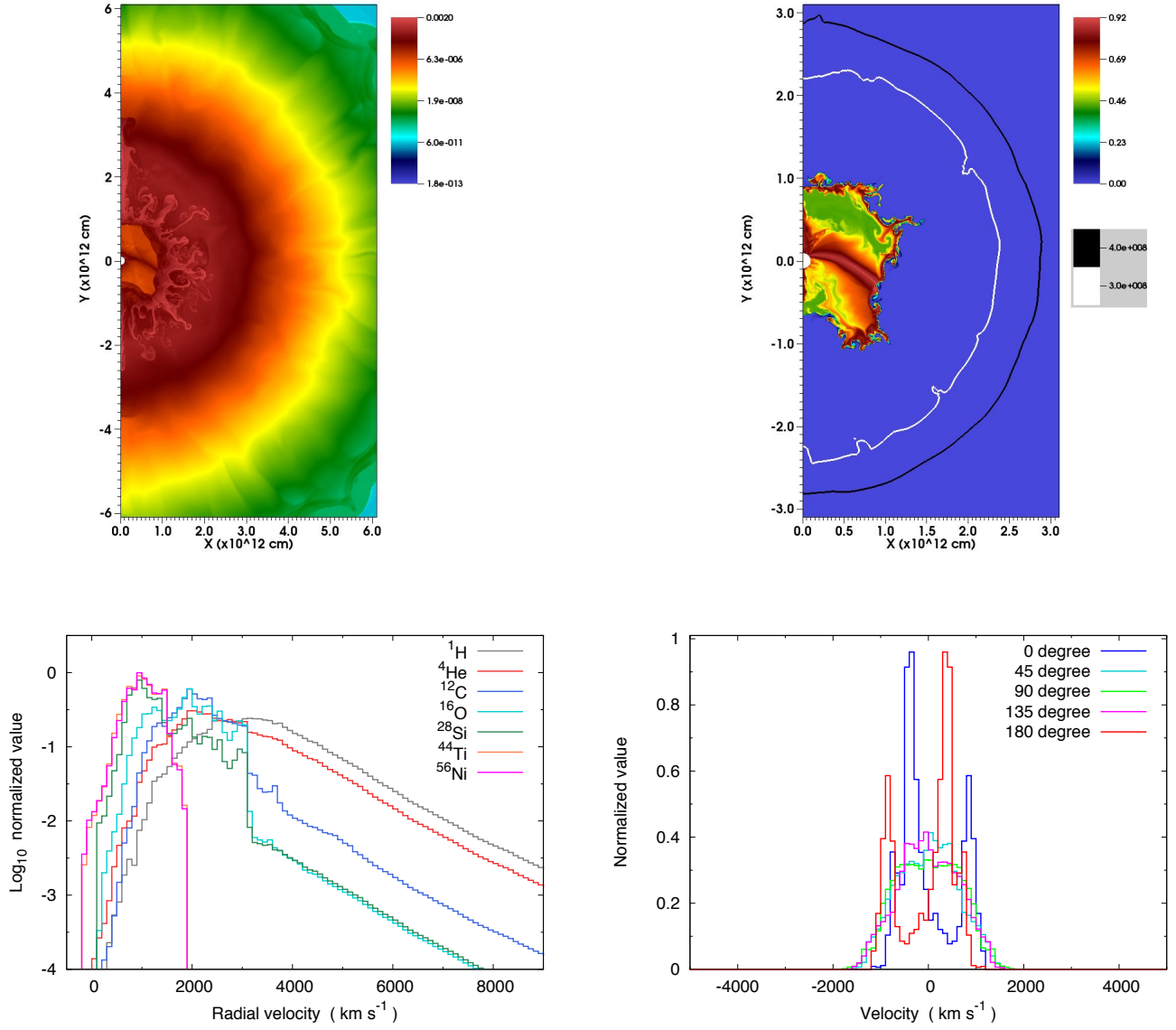


Fig. 12.— Results obtained from the model SC3p50f1. Panel descriptions are the same as those in Figure 3.

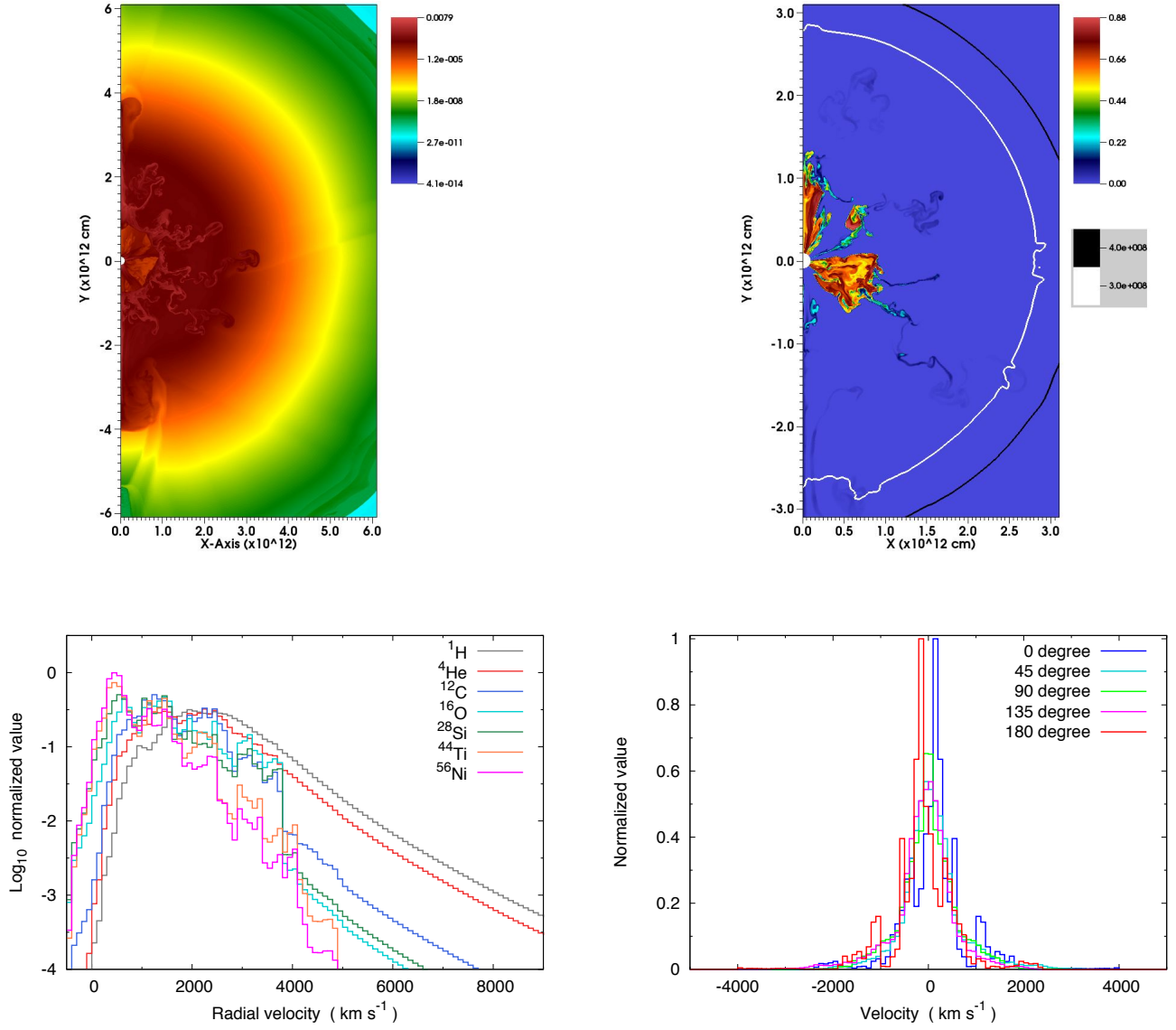


Fig. 13.— Results obtained from the model SC1p50m20(*). Panel descriptions are the same as those in Figure 3.

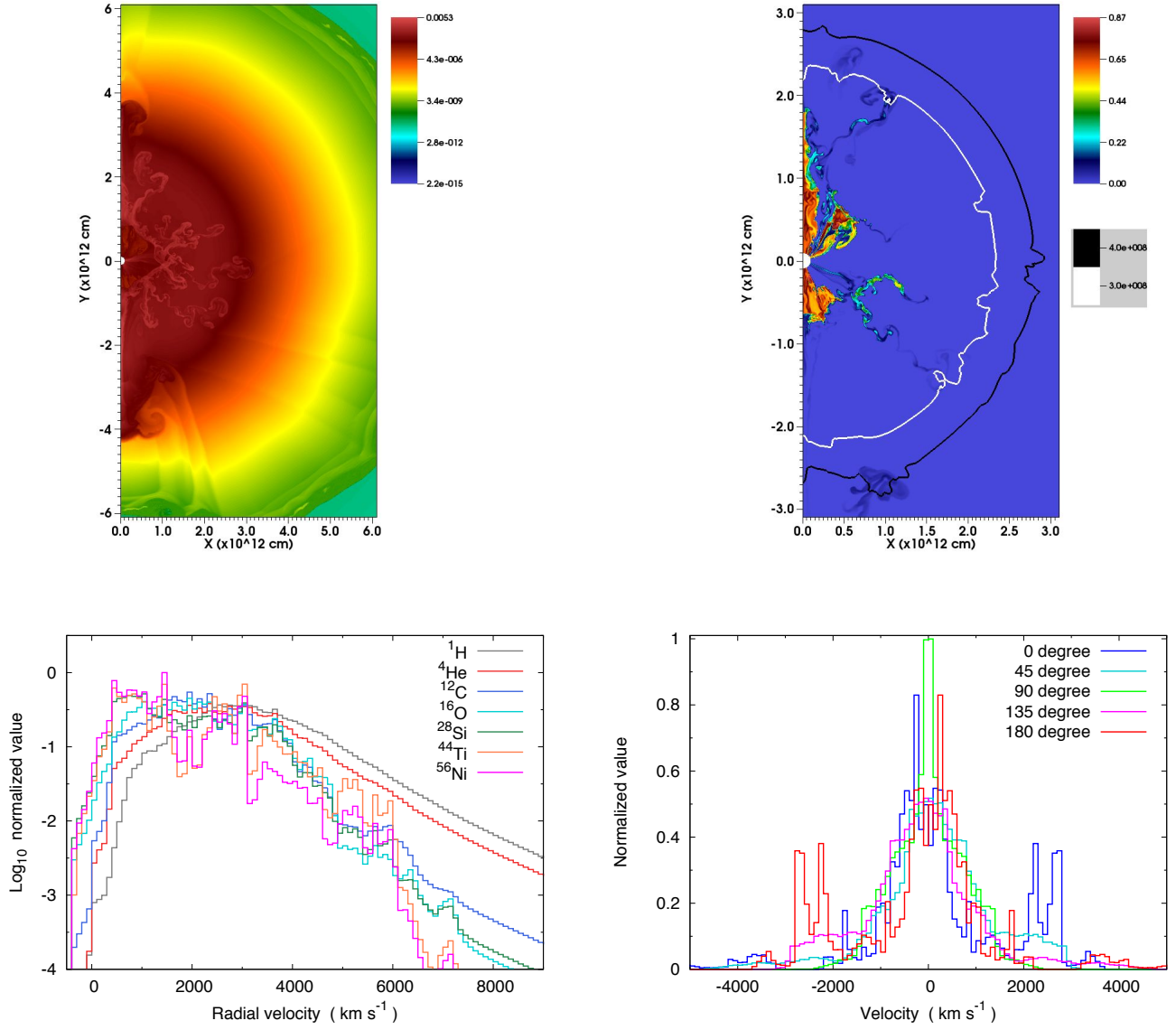


Fig. 14.— Results obtained from the model Bipo+SC1p50m20. Panel descriptions are the same as those in Figure 3.

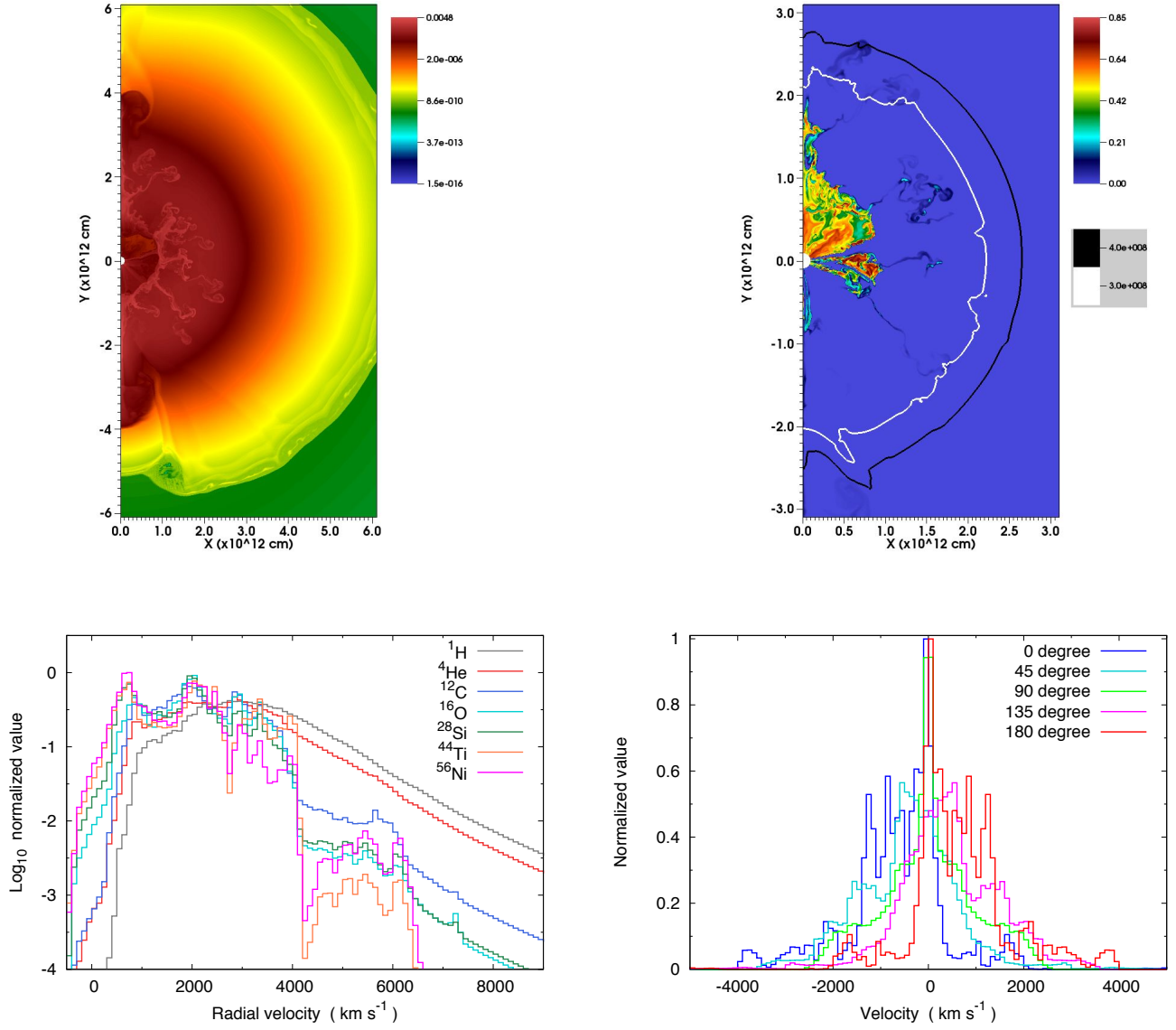


Fig. 15.— Results obtained from the model AsyEqua+SC1p50m20. Panel descriptions are the same as those in Figure 3.

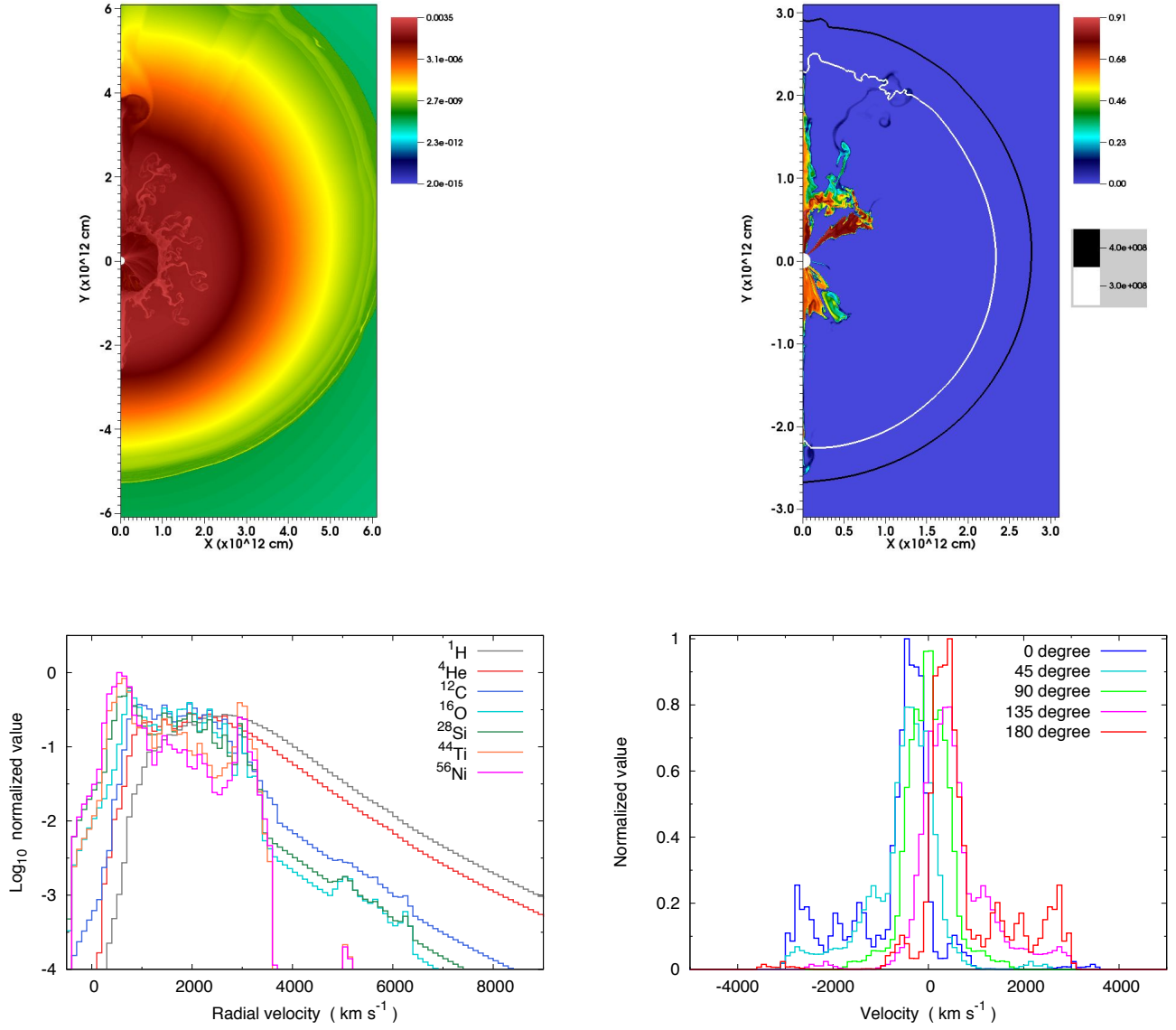


Fig. 16.— Results obtained from the model AspH+SC1p50m20(**). Panel descriptions are the same as those in Figure 3.

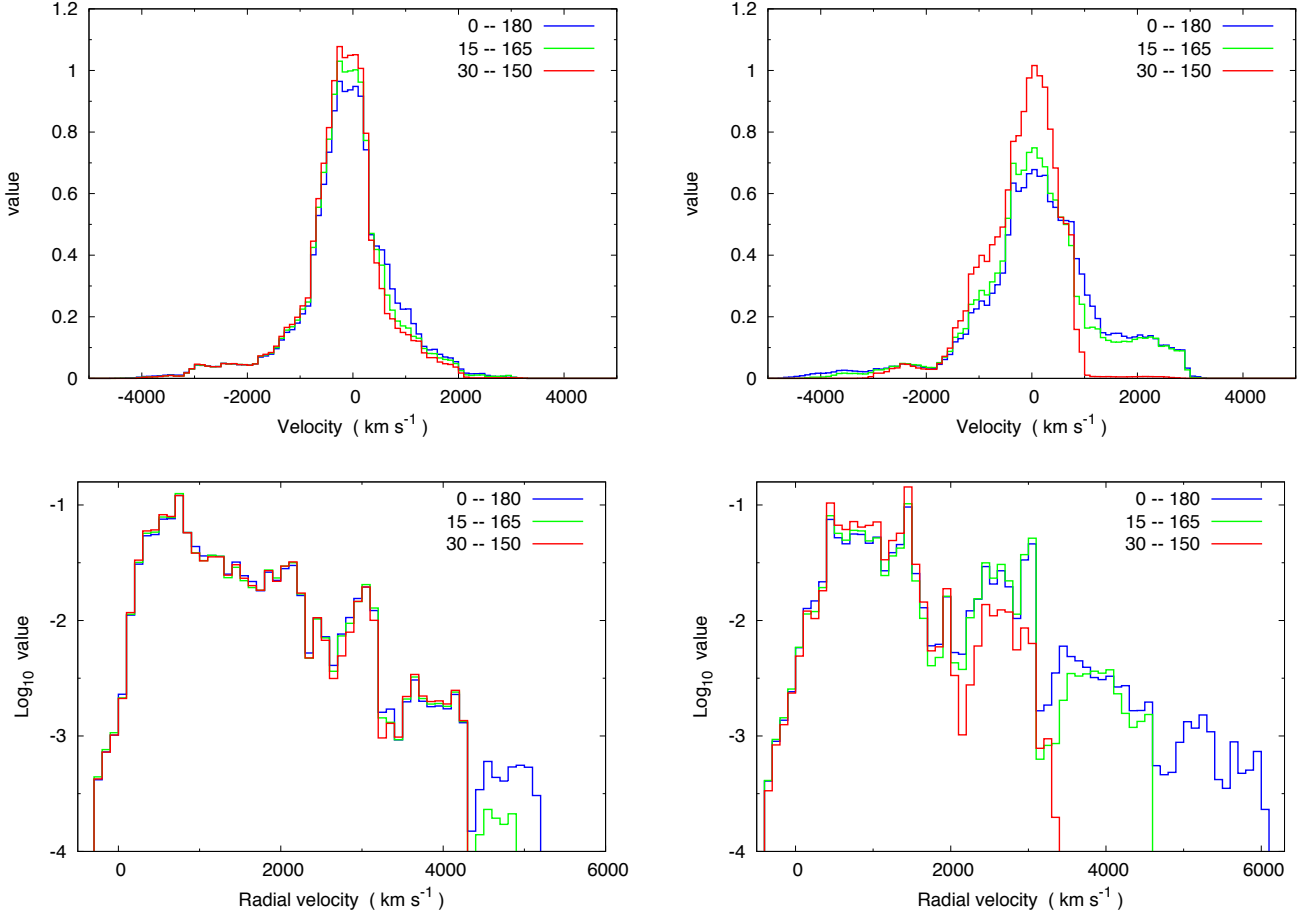


Fig. 17.— Line of sight velocity profiles and radial velocity profiles of ^{56}Ni for the simple test of the axis-jet effect. The labeled value in the y-axis of each panel is $\Delta M/M$ (without normalization), where ΔM is the mass in the velocity range of $v \sim v + \Delta v$, and M is the total mass. The view angle is 45 degree and the velocity bin is 100 km s^{-1} . Upper left: Line of sight velocity profiles of the model “SC1p50m20”; upper right: line of sight velocity profiles of the model “Bipo+C1p50m20”; lower left: radial velocity profiles of the model “SC1p50m20”; lower right: radial velocity profiles of the model “Bipo+C1p50m20”. In each panel, “0–180”, “15–165”, and “30–150” indicate the computational domain within the angular ranges of 0–180 degree, 15–165 degree, and 30–150 degree, respectively.

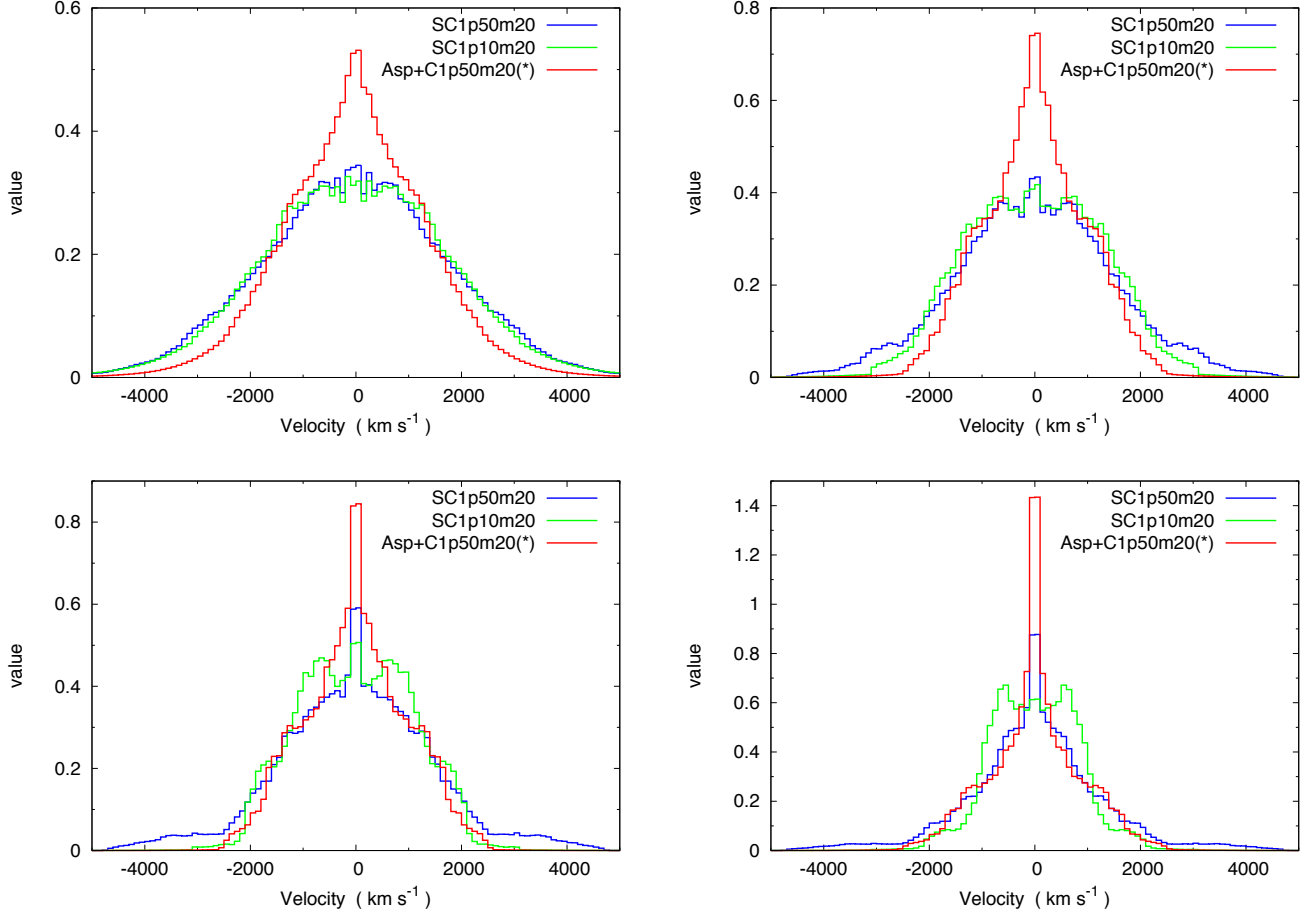


Fig. 18.— Line of sight velocity profiles of four elements. The view angle is 90 degree and the velocity bin is 100 km s^{-1} . Upper left: line of sight velocity profiles of ${}^4\text{He}$; upper right: line of sight velocity profiles of ${}^{12}\text{C}$; lower left: line of sight velocity profiles of ${}^{16}\text{O}$; lower right: line of sight velocity profiles of ${}^{28}\text{Si}$. The labeled value in the y-axis of each panel is $\Delta M/M$ (without normalization), where ΔM is the mass in the velocity range of $v \sim v + \Delta v$, and M is the total mass. Three models are considered in each panel: SC1p50m20 (spherical explosion with 50% of density perturbation), SC1p10m20 (spherical explosion with 10% of density perturbation), and Asp+C1p50m20(*) (aspherical explosion with 50% of density perturbation).

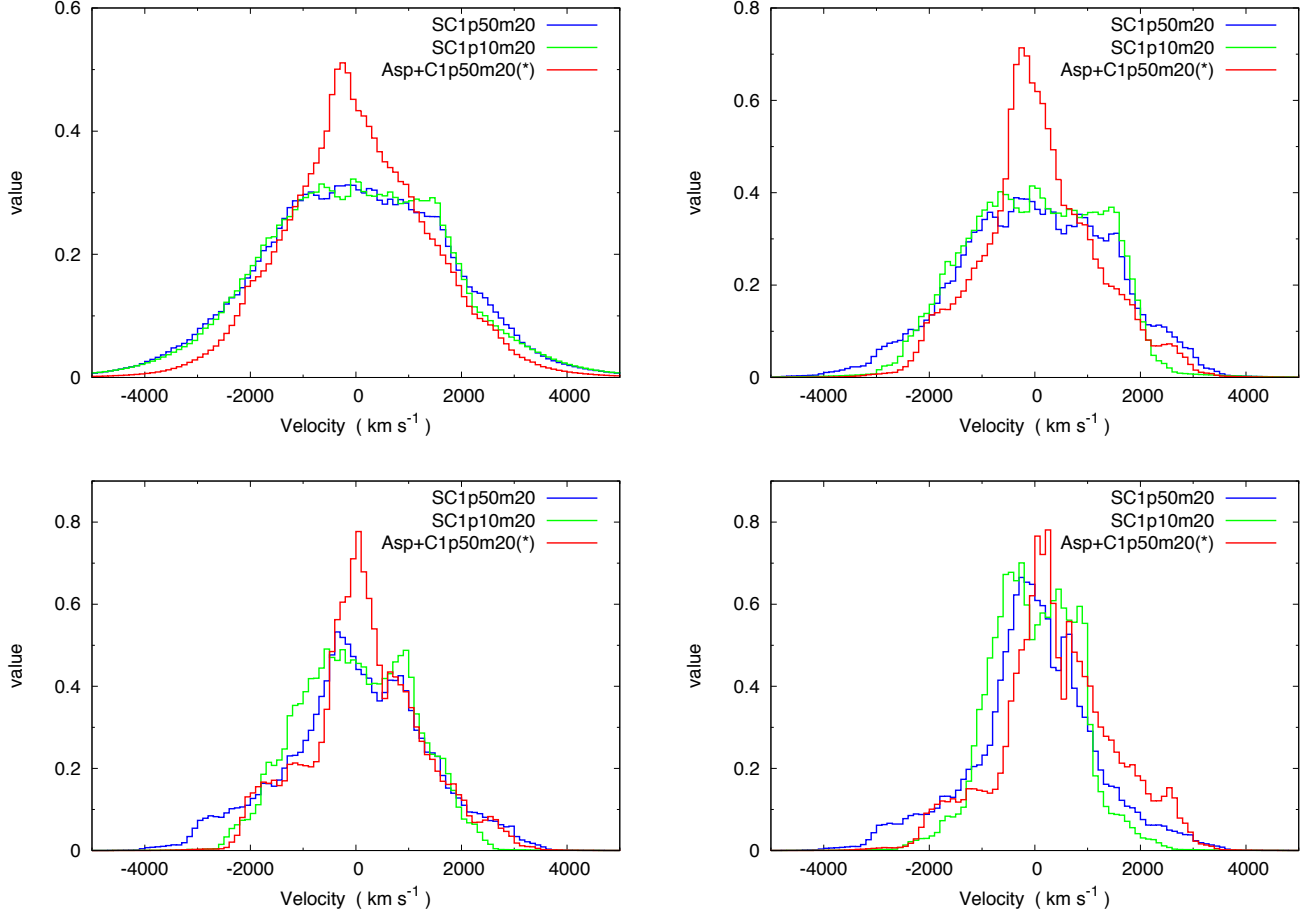


Fig. 19.— Line of sight velocity profiles of four elements. The view angle is 45 degree and the velocity bin is 100 km s^{-1} . Upper left: line of sight velocity profiles of ^4He ; upper right: line of sight velocity profiles of ^{12}C ; lower left: line of sight velocity profiles of ^{16}O ; lower right: line of sight velocity profiles of ^{28}Si . The labeled value in the y-axis of each panel is $\Delta M/M$ (without normalization), where ΔM is the mass in the velocity range of $v \sim v + \Delta v$, and M is the total mass. Three models are considered in each panel: SC1p50m20 (spherical explosion with 50% of density perturbation), SC1p10m20 (spherical explosion with 10% of density perturbation), and Asp+C1p50m20(*) (aspherical explosion with 50% of density perturbation).

Table 1: Parameters in simulation models

Model/Parameter	ϵ_0	m	f	$v_{\text{pol}}/v_{\text{eq}}$	$v_{\text{up}}/v_{\text{down}}$	Perturbation Position
Fiducialmodel	0.0	0	-	-	-	no perturbation
Basicmodel	0.5	20	-	-	-	4 critical radii
SC1p50m8	0.5	8	-	-	-	4 critical radii
SC1p50m8(\diamond)	0.5	8	-	-	-	4 critical radii
SC1p50m20	0.5	20	-	-	-	4 critical radii
SC1p50m20(*)	0.5	20	-	-	-	4 critical radii
SC1p10m8	0.1	8	-	-	-	4 critical radii
SC1p10m20	0.1	20	-	-	-	4 critical radii
SC1Si/C+O	0.5	20	-	-	-	Si/C+O interface
SC1C+O/He	0.5	20	-	-	-	C+O/He interface
SC1He/H	0.5	20	-	-	-	He/H interface
SC1C+O/He/H	0.5	20	-	-	-	C+O/He and He/H interfaces
SC2p50m8f5	0.5	8	5	-	-	radial & angular modulated
SC2p50m20f5	0.5	20	5	-	-	radial & angular modulated
SC2p10m8f5	0.1	8	5	-	-	radial & angular modulated
SC2p10m20f5	0.1	20	5	-	-	radial & angular modulated
SC2p50m20f1	0.5	20	1	-	-	radial & angular modulated
SC3p50f1	0.5	-	1	-	-	radial modulated
SC3p50f5	0.5	-	5	-	-	radial modulated
Bipo+C1p50m20	0.5	20	-	4.0	-	4 critical radii
AsyEqua+C1p50m20	0.5	20	-	-	1.8	4 critical radii
Asph+C1p50m20	0.5	20	-	4.0	1.8	4 critical radii
Asph+C1p25m20	0.25	20	-	4.0	1.8	4 critical radii
Asph+C1p10m20	0.10	20	-	4.0	1.8	4 critical radii
Asph+C1p50m20(*)	0.5	20	-	4.0	1.8	4 critical radii
Asph+C1p25m20(**)	0.25	20	-	4.0	1.8	4 critical radii

Note. — SC1, SC2, and SC3 are three spherical SN explosion cases presented in Section 2.3.1. Bipolar explosion is labeled as “Bipo” and equatorially asymmetric explosion is labeled as “AsyEqua”. The combination of bipolar and equatorially asymmetric explosions is labeled as “Asph”. The four critical radii in the CCSN progenitor are 3×10^8 cm at Si/C+O interface, 3×10^9 cm at oxygen shell burning position, 6×10^9 cm at C+O/He interface, and 5×10^{10} cm at He/H interface, respectively. ϵ_0 is the density perturbation amplitude, m is the wave number of perturbations in the angular direction, and f is the scaling factor of the perturbation length scale. The ratio of the initial radial velocity along the polar axis to that along the equatorial axis $v_{\text{pol}}/v_{\text{eq}}$ is given for bipolar explosion models. The ratio of the initial radial velocity $v_{\text{up}}/v_{\text{down}}$ at $\theta = 0$ to that at $\theta = \pi$ is given for equatorially asymmetric models. All models have input energies of 2.5×10^{51} erg; exceptions are those labeled by “*” in which we set the input energy to be 1.7×10^{51} erg and the one labeled by “**” in which we set the input energy to be 2.0×10^{51} erg. The model of SC1p50m8(\diamond) has a set of random numbers, which are different from the model of sc1p50m8.

Table 2: Main results of simulation models

Model/Result unit	Time (s)	Explosion (10^{51} erg)	$^{56}\text{Ni}_{\text{tot}}$ (M_{\odot})	$^{56}\text{Ni}_{\text{ratio}}$ (%)	$^{44}\text{Ti}_{\text{tot}}$ ($10^{-4}M_{\odot}$)	v_r^{max} (km s^{-1})	FigNo.
Fiducialmodel	6959	1.91	0.21	-	2.8	1700	-
Basicmodel	6982	1.87	0.19	-	3.5	2000	-
SC1p50m8	6577	1.80	0.14	23.1	2.7	4800	Fig. 3
SC1p50m8(\diamond)	6557	1.83	0.15	21.7	2.1	3700	Fig. 4
SC1p50m20	7062	1.84	0.17	5.6	7.2	4200	Fig. 5
SC1p50m20(*)	9006	1.08	0.13	0.9	3.2	4100	Fig. 13
SC1p10m8	6978	1.89	0.19	-	2.1	1700	-
SC1p10m20	7029	1.89	0.20	-	2.8	1500	Fig. 6
SC1Si/C+O	7005	1.87	0.18	-	5.5	1700	-
SC1C+O/He	7013	1.86	0.16	0.7	2.7	3100	-
SC1He/H	7196	1.88	0.19	0.6	2.6	2100	-
SC1C+O/He/H	7087	1.83	0.15	11.5	2.3	4800	Fig. 7
SC2p50m8f5	5785	2.01	0.18	8.3	3.0	3700	Fig. 8
SC2p50m20f5	6618	1.96	0.21	5.1	3.8	4200	Fig. 9
SC2p10m8f5	6762	1.94	0.21	-	3.0	1800	-
SC2p10m20f5	6892	1.93	0.21	-	3.0	1600	Fig. 10
SC2p50m20f1	6636	1.89	0.21	0.1	4.4	2800	Fig. 11
SC3p50f1	6964	1.88	0.20	-	3.2	1900	Fig. 12
SC3p50f5	6330	2.01	0.19	-	2.9	2000	-
Bipo+SC1p50m20	6714	1.87	0.09	10.6	6.9	6000	Fig. 14
AsyEqua+SC1p50m20	6365	1.88	0.12	7.0	9.4	6000	Fig. 15
Asph+SC1p50m20	6136	1.85	0.09	19.4	7.5	5300	-
Asph+SC1p25m20	6101	1.91	0.09	9.2	4.0	4200	-
Asph+SC1p10m20	6382	1.94	0.09	1.4	2.7	2100	-
Asph+SC1p50m20(*)	8133	1.11	0.06	10.0	4.9	4500	-
Asph+SC1p25m20(**)	6984	1.43	0.07	6.5	2.8	3400	Fig. 16

Note. — The physical time at which we stop the simulation is labeled as “Time” and the explosion energy is labeled as “Explosion”. The total masses of ^{56}Ni and ^{44}Ti are written as $^{56}\text{Ni}_{\text{tot}}$ and $^{44}\text{Ti}_{\text{tot}}$, respectively. All of these element mass values are calculated from the 2D FLASH code in which the limited nucleosynthesis network is adopted. The ratio of the high velocity ^{56}Ni ($> 3000 \text{ km s}^{-1}$) mass to the total mass of ^{56}Ni is written as $^{56}\text{Ni}_{\text{ratio}}$. The maximum radial velocity of ^{56}Ni corresponding to the value of $\Delta M/M$ larger than 1.0×10^{-3} in radial velocity profiles is labeled as v_r^{max} , where ΔM is the mass in the velocity range of $v \sim v + \Delta v$, and M is the total mass. “FigNo.” is the figure number corresponding to the related simulation model in this paper.

Table 3: Minimum and maximum radial velocities (v_r^{\min} and v_r^{\max}) of each element

Model/Result ^a Unit	$v_r^{\max}(^{56}\text{Ni})$ (km s ⁻¹)	$v_r^{\max}(^{44}\text{Ti})$ (km s ⁻¹)	v_r^{\min} & $v_r^{\max}(^{28}\text{Si})$ (km s ⁻¹)	v_r^{\min} & $v_r^{\max}(^{16}\text{O})$ (km s ⁻¹)	v_r^{\min} & $v_r^{\max}(^{12}\text{C})$ (km s ⁻¹)	v_r^{\min} & $v_r^{\max}(4\text{He})$ (km s ⁻¹)	$v_r^{\min}(\text{H})$	FigNo. ^b
Fiducialmodel	1700	1700	1300 & 1600	1300 & 1800	1400 & 4600	1500 & 6700	1900	-
Basicmodel	2000	2000	300 & 3000	600 & 3000	700 & 4400	700 & 6700	800	-
SC1p50m8	4800	4800	0 & 4800	300 & 4300	700 & 4900	700 & 6400	900	Fig. 3
SC1p50m8(\diamond)	3700	3700	0 & 3800	300 & 3800	500 & 4500	500 & 6000	700	Fig. 4
SC1p50m20	4200	4500	-100 & 4700	-200 & 4700	500 & 5100	500 & 6600	600	Fig. 5
SC1p50m20(*)	4100	4000	-300 & 3700	-100 & 3700	200 & 3800	200 & 5300	400	Fig. 13
SC1p10m8	1700	1700	900 & 2300	1000 & 2500	1100 & 4500	1100 & 6700	1400	-
SC1p10m20	1500	1500	600 & 3100	800 & 3100	900 & 4500	800 & 6700	1000	Fig. 6
SC1Si/C+O	1700	1700	900 & 2100	1100 & 2200	1200 & 4500	1200 & 6700	1500	-
SC1C+O/He	3100	3100	400 & 3200	700 & 3200	800 & 4500	800 & 6700	1000	-
SC1He/H	2100	2100	300 & 4800	300 & 4800	600 & 5500	400 & 6600	700	-
SC1C+O/He/H	4800	4800	200 & 4800	400 & 4900	500 & 5300	600 & 6500	600	Fig. 7
SC2p50m8f5	3700	3700	-100 & 3700	300 & 5600	400 & 5800	400 & 6900	700	Fig. 8
SC2p50m20f5	4200	4600	400 & 4600	500 & 4600	500 & 5400	500 & 6800	700	Fig. 9
SC2p10m8f5	1800	1800	1000 & 2300	1100 & 2800	1200 & 4600	1100 & 6800	1400	-
SC2p10m20f5	1600	1500	500 & 3300	600 & 3400	800 & 4500	700 & 6800	900	Fig. 10
SC2p50m20f1	2800	2700	600 & 3700	700 & 3900	700 & 5000	600 & 6700	900	Fig. 11
SC3p50f1	1900	1800	100 & 3100	400 & 3100	700 & 4700	600 & 6800	900	Fig. 12
SC3p50f5	2000	2000	800 & 2200	1000 & 2200	1200 & 4800	1300 & 7400	1900	-
Bipo+SC1p50m20	6000	6000	-400 & 6400	-400 & 6400	0 & 7100	0 & 9800	300	Fig. 14
AsyEqua+SC1p50m20	6000	5600	-400 & 6300	-400 & 6300	200 & 7200	200 & 9900	500	Fig. 15
Asph+SC1p50m20	5300	5300	0 & 5300	0 & 5300	200 & 5300	300 & 6600	600	-
Asph+SC1p25m20	4200	4300	-200 & 3900	200 & 3900	500 & 4400	500 & 6800	800	-
Asph+SC1p10m20	2100	3500	100 & 3800	400 & 3800	800 & 4500	800 & 6800	1100	-
Asph+SC1p50m20(*)	4500	3900	-400 & 3900	-400 & 3800	-100 & 4100	0 & 5400	400	-
Asph+SC1p25m20(**)	3400	3400	-300 & 3400	-100 & 3300	400 & 4000	400 & 6000	700	Fig. 16

^aThe minimum and maximum radial velocity of each element corresponds to the value of $\Delta M/M$ larger than 1.0×10^{-3} in radial velocity profiles, where ΔM is the mass in the velocity range of $v \sim v + \Delta v$, and M is the total mass.

^bFigNo. is the figure number corresponding to the related simulation model in this paper.